PCH-2^{TRIP13} regulates spindle checkpoint strength

Lénaïg Défachelles, Anna E. Russo, Christian R. Nelson and Needhi Bhalla*

Department of Molecular, Cell and Developmental Biology, University of California, Santa Cruz,

Santa Cruz, CA 95064

*corresponding author: nbhalla@ucsc.edu

Department of Molecular, Cell and Developmental Biology

225 Sinsheimer Labs

University of California, Santa Cruz

Santa Cruz, CA 95064

phone: (831) 459-1319

fax: (831) 459-3139

Key words: *C. elegans*, mitosis, embryo, spindle assembly checkpoint, Mad2, aneuploidy, germline

ABSTRACT

Spindle checkpoint strength, defined as the length of the cell cycle delay imposed by the spindle checkpoint, is dictated by three criteria: the number of unattached kinetochores, cell volume and cell fate. However, how checkpoint strength is regulated is unknown. We show that the conserved AAA-ATPase, PCH-2, which remodels the essential checkpoint effector Mad2 from an active conformation to an inactive one, controls checkpoint strength in *C. elegans*. When we genetically manipulate embryos to decrease cell volume, PCH-2 is no longer required for the spindle checkpoint or recruitment of Mad2 at unattached kinetochores, showing that PCH-2 is essential for a robust checkpoint in large cells. This role in checkpoint strength is not limited to large cells: germline precursor cells exhibit a stronger checkpoint than their somatic counterparts and this also relies on PCH-2. PCH-2 is more highly enriched in germline precursor cells than in somatic cells and this enrichment relies on a conserved factor that induces asymmetry in the early embryo. Finally, the stronger checkpoint in germline precursor cells also depends on CMT-1, which is essential for both PCH-2's localization to unattached kinetochores and its enrichment in germline precursor cells. Thus, PCH-2's ability to regulate the availability of an inactive but necessary checkpoint precursor at or near unattached kinetochores governs checkpoint strength.

INTRODUCTION

To prevent the missegregation of chromosomes and the production of daughter cells with an incorrect number of chromosomes, the spindle checkpoint (also called the spindle assembly checkpoint) monitors whether chromosomes are attached to the spindle via kinetochores. If kinetochores fail to attach properly, this checkpoint delays the cell cycle to promote error correction and prevent aneuploidy. Despite its critical role, the strength of the spindle checkpoint, defined as the duration of the cell cycle delay, can be highly variable. This variability is controlled by the number of unattached kinetochores (Collin et al., 2013), cell volume, (Kyogoku and Kitajima, 2017; Galli and Morgan, 2016) and cell fate (Galli and Morgan, 2016; Gerhold et al., 2018).

The spindle checkpoint response initiates with the recruitment of Mad1 and Mad2 at unattached kinetochores (Sironi et al., 2001), which catalyzes the production of a Mitotic Checkpoint Complex (MCC) (Chen et al., 1996; Li and Benezra, 1996; Chen et al., 1998). The MCC enforces a checkpoint arrest by inhibiting the Anaphase Promoting Complex/Cyclosome (APC/C) and preventing cell cycle progression (Sudakin et al., 2001). Formation of the MCC is driven by conformational changes in Mad2, which can exist in an open conformation (O-Mad2) or a closed conformation (C-Mad2) (Luo et al., 2002; Sironi et al., 2002; Luo et al., 2004). Mad2 is in the closed conformation in the Mad1/Mad2 tetramer recruited to unattached kinetochores. C-Mad2 in the tetramer acts as a template to convert additional soluble O-Mad2 to C-Mad2, which can be assembled into the MCC (Sironi et al., 2001; De Antoni et al., 2005; Fava et al., 2011). Thus, unattached kinetochores act as a platform for MCC assembly. The MCC effectively tunes the spindle checkpoint response: the length of the cell cycle delay imposed by the

71 checkpoint is governed by the ratio of the soluble MCC checkpoint signal to cytoplasmic
72 volume (Collin et al., 2013; Dick and Gerlich, 2013).
73
74 PCH-2, known as TRIP13 in mammals, is a hexameric AAA+ ATPase that remodels
75 HORMA domain-containing proteins, a group that includes Mad2 (Aravind and Koonin,
76 1998; Chen et al., 2014; Vader, 2015; Ye et al., 2015). Originally described as a spindle
77 checkpoint silencing protein, experiments showed that TRIP13 works with the adaptor
78 protein p31^{comet} to extract C-Mad2 from the MCC and promote its disassembly,
79 permitting the activation of the APC/C (Wang et al., 2014; Eytan et al., 2014; Ye et al.,
80 2015; Miniowitz-Shemtov et al., 2015; Brulotte et al., 2017; Alfieri et al., 2018). We and
81 others have shown that PCH-2/TRIP13 is essential for spindle checkpoint activation in
82 *C. elegans* and mammalian cells (Nelson et al., 2015; Ma and Poon, 2016; Yost et al.,
83 2017). PCH-2 is present at unattached kinetochores (Tipton et al., 2012; Wang et al.,
84 2014; Nelson et al., 2015) and is required to robustly localize Mad2, but not Mad1, to
85 unattached kinetochores (Nelson et al., 2015; Yost et al., 2017). Biochemical and
86 structural studies have shown that PCH-2 converts C-Mad2 to O-Mad2 (Ye et al., 2015;
87 Brulotte et al., 2017; Alfieri et al., 2018). Altogether, these data suggest a model in which
88 PCH-2 converts a population of C-Mad2 that is not competent for checkpoint signaling
89 into O-Mad2, so that Mad1/Mad2 recruited to unattached kinetochores can template C-
90 Mad2 for assembly into the MCC.
91
92 This model has major implications for our understanding of the spindle checkpoint. First,
93 it indicates that the spindle checkpoint does not simply depend on the presence of C-
94 Mad2. Rather, only C-Mad2 that has been assembled into the MCC at unattached
95 kinetochores is competent for checkpoint signaling (Ma and Poon, 2016). Second, it
96 suggests that there is a significant population of C-Mad2 in cells that must be liberated

97 for a functional checkpoint. In *C. elegans*, some of this C-Mad2 appears to be
98 complexed with and stabilized by the Mad2 mimic p31^{comet} (CMT-1 in *C. elegans*) (Yang
99 et al., 2007; Nelson et al., 2015); loss of CMT-1 partially suppresses the spindle
100 checkpoint defect in *pch-2* mutants, likely by liberating enough O-Mad2 to make PCH-2
101 partially dispensable (Nelson et al., 2015). In cells that have a significant population of
102 available O-Mad2, such as HeLa cells (Luo et al., 2004), TRIP13 function becomes
103 essential for checkpoint activity only when this population of O-Mad2 is limiting (Ma and
104 Poon, 2018).
105
106 Here, we show that PCH-2's role in regulating the availability of O-Mad2 controls spindle
107 checkpoint strength in *C. elegans*. Despite being essential for the spindle checkpoint in
108 the large somatic, or AB, cell of the two-cell embryo, PCH-2 becomes dispensable as AB
109 cells are genetically manipulated to become smaller, suggesting that PCH-2's ability to
110 concentrate O-Mad2 near unattached kinetochores is essential for checkpoint activation
111 in large cells. Indeed, as AB cells become smaller PCH-2 is also dispensable for Mad2
112 recruitment at unattached kinetochores. This requirement in promoting spindle
113 checkpoint strength is also observed in germline precursor, or P_1, cells, which have a
114 stronger checkpoint than their somatic counterparts. PCH-2 is enriched in P_1 cells and
115 this enrichment is dependent on a conserved regulator of embryonic polarity, PAR-1.
116 Further, the stronger checkpoint in P_1 cells also relies on the *C. elegans* ortholog of
117 p31^{comet}, CMT-1, suggesting that CMT-1's role in localizing PCH-2 to unattached
118 kinetochores and/or its ability to enrich PCH-2 in P_1 cells, contributes to a stronger
119 checkpoint. We propose that in scenarios where maintaining genomic stability can be
120 particularly challenging and/or relevant, such as in oocytes and early embryos enlarged
121 for developmental competence and germline cells that maintain immortality, PCH-2, and

122 its mammalian ortholog TRIP13, ensure a robust spindle checkpoint response and
123 proper chromosome segregation.
124
125 **MATERIALS AND METHODS**
126
127 **Worms strains**
128 The *C. elegans* Bristol N2 (Brenner, 1974) was used as the wild-type strain. All strains
129 were maintained at 20°C. See Table S1 for the list of all the strains used in this study.
130
131 **Immunostaining**
132 Immunostaining was performed on adult worms 48h after L4, as described in (Bhalla and
133 Dernburg, 2005). The antibodies used were rabbit anti-MAD-2 (1/500; Essex et al.,
134 2009) and mouse anti-MAb414 (1/400; Davis and Blobel, 1986). Secondary antibodies
135 were Alexa Fluor 488 anti-rabbit (Invitrogen) and Cy3 anti-mouse (Jackson
136 ImmunoResearch Laboratories, Inc.) diluted at 1:500. Antibody against MAD-2 was a gift
137 from A. Desai (Ludwig Institute/University of California, San Diego, La Jolla, CA).
138
139 Images were acquired on a DeltaVision Personal DV microscope (GE Healthcare)
140 equipped with a 100× NA 1.40 oil-immersion objective (Olympus), a short ARC xenon
141 lamp (GE Healthcare) and using a CoolSNAP charge-coupled camera (Roper Scientific).
142 Z-stacks were collected at 0.2 µm Z-spacing and processed by constrained, iterative
143 deconvolution. Imaging, image scaling, and analysis were performed using functions in
144 the softWoRx software package (GE Healthcare). Projections were calculated by a
145 maximum intensity algorithm. Composite images were assembled and some false
146 coloring was performed with Fiji.
147

148 **Live imaging of two-cell embryos**

149 For live imaging of two-cell embryos, worms were dissected on glass coverslips in egg
150 buffer and then mounted on 2% agar pads. Images were acquired every 1 minute or 20
151 seconds on a DeltaVision Personal DV microscope as described in the previous section;
152 except that the distance between two planes was 2 µm. The mitotic timing was
153 measured from NEBD to OCC as described in (Nelson et al., 2015). Cell volumes were
154 measured as described in (Galli and Morgan, 2016). To measure the nuclear area, a
155 sum projection of the embryo was generated 1 minute before chromosomes began to
156 condense and the area was measured with Fiji (Figure S2A).

157

158 **Live imaging of embryogenesis**

159 After a treatment with *perm-1*^{RNAi} (see below), worms were dissected onto a coverslip
160 with egg salt buffer (118 mM NaCl, 48 mM KCl) supplemented with 10 mM PIPES pH
161 7.3, 1 mM ATP and 10 mM sucrose. Embryos and adult carcasses were transferred into
162 a well of an 8-well plate (ibidi 1 µ-Slide 8 Well Glass bottom) that had been freshly
163 coated with 0.1% Poly-L-Lysine solution (Sigma P8920) and extensively washed. Time-
164 lapse videos were acquired with a Solamere spinning disk confocal system piloted by
165 µManager software (Edelstein et al., 2014) and equipped with a Yokogawa CSUX-1
166 scan head, a Nikon (Garden City, NY) TE2000-E inverted stand, a Hamamatsu
167 ImageEM ×2 camera, LX/MAS 489 nm and LS/MAS 561 nm laser, and Plan Apo
168 ×60/1.4 numerical aperture oil objective. Acquisition times per frame were 50 ms using
169 5% of the lasers power for both channels, and images were obtained as stacks of planes
170 at 2 µm intervals taken every 1 minute. Nocodazole was added from a 5X stock to a final
171 concentration of 50 µM after the first time point.

172

173 **Quantification of fluorescence intensity**

174 To quantify GFP::MAD-2 and PCH-2::GFP levels, images were generated under the
175 same conditions as previously described for the live imaging of two-cell embryos with a
176 few modifications: only the nucleus was imaged, the interval between two planes was 1
177 µm and images were collected every 20 seconds. To measure the cell volume, one Z-
178 stack of the entire cell was taken at NEBD at 2 µm Z-spacing.
179 Quantification of fluorescence at kinetochores or around mitotic chromosomes was
180 performed in Fiji as described in (Moyle et al., 2014; Nelson et al., 2015) and
181 fluorescence in the cytoplasm as describes in (Galli and Morgan, 2016).
182
183 **Feeding RNAi**
184 *C. elegans* strains were fed HT115 bacteria expressing the desired dsRNA after IPTG
185 induction. Bacterial strains containing RNAi vectors were cultured overnight at 37°C,
186 centrifuged, and the pellet was resuspended in 1/50 of the original volume. 100 µl of
187 concentrated culture was spotted onto a nematode growth medium (NGM) plate
188 containing 1 mM IPTG and 50 µg/µl of kanamycin or carbenicillin and the plate was
189 incubated overnight at 37°C.
190
191 For *ani-2*^{RNAi}, gravid adults were bleached onto the RNAi plate and their progeny was
192 allowed to develop at 20°C during 2.5 days. Then, L4s were transferred to a fresh plate
193 containing OP50 or *zyg-1*^{RNAi} bacteria.
194
195 For *zyg-1*^{RNAi}, L4s were transferred (from an OP50 or ani-2^{RNAi} plate) onto a *zyg-1*^{RNAi}
196 plate and cultured 1.5 days at 20°C.
197
198 For *perm-1*^{RNAi}, young adults (8h post L4) were incubated onto *perm-1*^{RNAi} plates for 16-
199 20h at 15°C.

200

201 For *par-1*^{RNAi}, gravid adults were bleached onto control RNAi (L4440) plates and their
202 progeny were allowed to develop at 15°C for 3 days. L4s were then transferred onto *par-*
203 *1*^{RNAi} or control RNAi (L4440) plates and incubated at 15°C for 3 days.

204

205 **Statistical Analysis**

206 Linear regression analysis and assessing significance of this data (Figures 1C, 4A, 4B,
207 S1B, S1D) was performed using GrapPad Prism version 6 for Macintosh. For all other
208 data, significance was assessed by performing t-tests (Figures 1D, 2C, 3, 4C, 5A, 5C,
209 5D, 6A, 6C, 6D, S3B, S3D, and S4B). In all graphs, a * indicates a p value < 0.05, **
210 indicates a p value < 0.01 and *** a p value < 0.0001.

211

212 **RESULTS**

213

214 **PCH-2 becomes dispensable for the spindle checkpoint response in somatic cells**
215 **as they decrease in size**

216 In the large somatic, or AB, cell of the *C. elegans* two-cell embryo, PCH-2 is essential for
217 spindle checkpoint activation (Nelson et al., 2015). To further assess the requirements
218 for PCH-2 function, we manipulated the cell volume of AB cells experimentally by
219 performing RNA interference (RNAi) against *ani-2*. *ani-2* encodes a germline specific
220 anillin whose depletion generates oocytes and, after fertilization, embryos, of varying
221 size (Maddox et al., 2005) (Figure 1A). We monitored the length of mitosis in these
222 embryos, using the time between nuclear envelope breakdown (NEBD) to the onset of
223 cortical contractility (OCC) as markers for the entry into and exit from mitosis,
224 respectively (Essex et al., 2009). We then correlated the length of mitosis to cytoplasmic
225 volume. RNAi of *ani-2* did not affect cell cycle progression in control, *pch-2*, or *mad-1*

226 mutants (Figure S1A), indicating that reducing cytoplasmic volume did not affect mitotic
227 timing in these embryos.
228
229 We performed double depletion of *ani-2* and *zyg-1* to induce the spindle checkpoint
230 response in control embryos, *pch-2*, and *mad-1* mutants. ZYG-1 is essential for
231 centrosome duplication after the first embryonic division, its depletion generates
232 monopolar spindles (O'Connell et al., 2001) and unattached kinetochores (Essex et al.,
233 2009) (Figure 1B). Consistent with previous reports, as cells decreased in cell volume
234 the length of the cell cycle delay, an indicator of spindle checkpoint strength, increased
235 in control embryos (Galli and Morgan, 2016; Gerhold et al., 2018) (Figure 1C).
236 Surprisingly, as *pch-2* mutant embryos decreased in size, the spindle checkpoint
237 response more closely resembled that of similarly sized control embryos than similarly
238 sized *mad-1* mutant embryos (Figure 1C). There was no significant difference between
239 the slopes of the regression analysis of control and *pch-2* mutant data (p value =
240 0.1407), while the slopes between the regression analysis of *pch-2* and *mad-1* mutant
241 data were significantly different (p value = 0.0007). We binned our data and observed
242 that *pch-2* mutant embryos fell into three clear categories: 1) wild-type sized embryos
243 (more than 5 x 10^3 μm^3) in which PCH-2 was essential for the spindle checkpoint; 2)
244 medium sized embryos (between 3.5 x 10^3 μm^3 and 5 x 10^3 μm^3), which exhibited an
245 intermediate level of checkpoint function; and 3) small embryos (less than 3.5 x
246 10^3 μm^3), in which PCH-2 was completely dispensable for the spindle checkpoint
247 response (Figure 1D).
248
249 We verified that the mitotic delay observed in *pch-2* embryos was a legitimate spindle
250 checkpoint response by monitoring mitotic timing after performing double depletion of
251 *ani-2* and *zyg-1* in *san-1* and *pch-2;san-1* mutant embryos. SAN-1 is the *C. elegans*

252 ortholog of the essential spindle checkpoint factor, Mad3 (Nystul et al., 2003) (Figure
253 S1B). There was no significant difference between the slopes of the regression analysis
254 of *san-1* and *pch-2;san-1* data (p value = 0.8813). These data allow us to draw two
255 important conclusions: 1) Since we observe a robust spindle checkpoint activation in
256 *pch-2* mutant embryos as they decrease in size and mitotic timing is similar to what we
257 observe in control embryos, PCH-2 does not appear to affect spindle checkpoint
258 silencing in *C. elegans*; and 2) PCH-2's requirement during spindle checkpoint activation
259 is proportional to cell volume in somatic cells of two-cell *C. elegans* embryos.
260
261 **PCH-2 becomes dispensable for MAD-2 recruitment at unattached kinetochores in**
262 **somatic cells as they decrease in size**
263 Recent experiments have shown that acute depletion of PCH-2's mammalian ortholog,
264 TRIP13, has no effect on spindle checkpoint function in HeLa cells until O-Mad2 is
265 limiting (Ma and Poon, 2018). Since MAD-2 is localized to the nucleus and nuclear
266 envelope in *C. elegans* oocytes (Bohr et al., 2015; Lawrence et al., 2015) (Figure 2A)
267 and *ani-2*^{RNAi} treatment does not affect nuclear size (Figure S2), we reasoned that as
268 cells decrease in cell volume, the absolute amount of MAD-2 protein is likely to remain
269 constant but its concentration increases. This increase in concentration may improve the
270 likelihood that O-Mad2 is at or near unattached kinetochores, obviating the requirement
271 for PCH-2 in small embryos.
272
273 To test this model, we quantified MAD-2 recruitment at unattached kinetochores in
274 pseudo-metaphase in small control and *pch-2* mutant embryos (less than 3.5 x 10^3 μm^3)
275 expressing GFP::MAD-2 and compared it to the recruitment observed in wild-type sized
276 embryos. Consistent with our previous results, GFP::MAD-2 was recruited to 20% of
277 control levels in *pch-2* mutant embryos that were wild-type in size (Nelson et al., 2015)

278 (Figure 2C). In small embryos, GFP::MAD-2 was recruited to unattached kinetochores in
279 control embryos as expected (Figure 2B). In small *pch-2* mutant embryos, GFP::MAD-2
280 signal can be detected at unattached kinetochores (Figure 2B) and, when quantified,
281 GFP::MAD-2 was partially restored to 58% of control levels (Figure 2C). One explanation
282 for why GFP::MAD-2 recruitment is not completely restored in small *pch-2* mutant
283 embryos may be that these smaller embryos require less MAD-2 recruitment to support
284 a mitotic delay comparable to control small embryos (Défachelles et al., 2015).
285 Nonetheless, our experiments demonstrate that PCH-2 is also dispensable for Mad2
286 recruitment at unattached kinetochores in small embryos, potentially because
287 decreasing cell volume concentrates Mad2, specifically O-Mad2.
288
289 **PCH-2 is required for the spindle checkpoint response during embryogenesis**
290 During embryogenesis, cell volume decreases and spindle checkpoint strength
291 increases (Galli and Morgan, 2016; Gerhold et al., 2018). Given our observation, that
292 PCH-2 becomes dispensable as cell volume decreases in the AB cell of two-cell
293 embryos, we tested whether this also happens during normal embryogenesis. We
294 permeabilized embryos by performing *perm-1* RNAi (Carvalho et al., 2011) and activated
295 the spindle checkpoint by treating these *perm-1*^{RNAi} embryos with nocodazole, a drug
296 that depolymerizes microtubules. Since we could not always reliably visualize OCC in
297 these dividing embryos, we measured mitotic timing from nuclear envelope break down
298 (NEBD) to the nuclear envelope reformation (NER) for each stage of embryogenesis.
299 Consistent with previous reports, cells in control embryos exhibited a longer mitotic delay
300 in 16-cell than in 4-cell embryos, indicating that the spindle checkpoint increases in
301 strength as cells decrease in volume during embryogenesis (Galli and Morgan, 2016;
302 Gerhold et al., 2018). As a control, we performed the same experiment in *san-1* mutants
303 and did not detect a mitotic delay when these embryos were treated with nocodazole

304 (Figure 3A). In stark contrast to our *ani-2*^{RNAi} experiments, the mitotic timing observed in
305 *pch-2* mutant embryos treated with nocodazole was similar to *san-1* mutant embryos
306 treated with nocodazole. Thus, as cells naturally decrease in cell size during
307 embryogenesis, PCH-2 remains essential for the spindle checkpoint.
308
309 We also tested if a subtle increase in MAD-2 protein levels would suppress the spindle
310 checkpoint defect in *pch-2* mutant embryos. The presence of a GFP::MAD-2 transgene,
311 in addition to endogenous MAD-2, results in about 2.5 times more MAD-2 in embryos.
312 This slight overexpression generates a normal spindle checkpoint response in control
313 AB cells and can bypass the requirement for checkpoint components MAD-3 or BUB-3
314 (Essex et al., 2009), but not PCH-2 (Nelson et al., 2015). We found that overexpression
315 of MAD-2 in control and *pch-2* mutant 4- and 16-cell embryos treated with nocodazole
316 behaved similarly as their counterparts with normal levels of MAD-2 (Figure 3B). These
317 results confirm that PCH-2 is essential for the spindle checkpoint during normal
318 embryogenesis, suggesting that Mad2 may undergo additional regulation during
319 embryogenesis that requires PCH-2 to make O-Mad2 available even as cells decrease
320 in size. Further, additional considerations may make direct comparisons between our
321 *ani-2*^{RNAi}*;zyg-1* ^{RNAi} experiments and dividing embryos treated with nocodazole difficult
322 (see Discussion).
323
324 **PCH-2 is responsible for the stronger spindle checkpoint in the germline lineage**
325 Cell fate is another important determinant of spindle checkpoint strength. In *C. elegans*
326 embryos, the spindle checkpoint is stronger in germline precursor cells than similarly
327 sized somatic counterparts (Galli and Morgan, 2016; Gerhold et al., 2018).
328 Therefore, we tested whether PCH-2 contributed to the stronger spindle checkpoint in
329 the germline lineage, specifically in P_1 cells of two-cell embryos (Figure 4). Consistent

330 with other reports (Galli and Morgan, 2016; Gerhold et al., 2018), when we performed
331 double depletion of *ani-2* and *zyg-1* in control embryos and monitored mitotic timing, we
332 observed P_1 cells with similar volumes as AB cells exhibiting a longer cell cycle delay
333 (Figure 4A). Further, the regression analysis that best fit control P_1 data is significantly
334 different and steeper than that of control AB cells (p value < 0.0001), suggesting that
335 variables in addition to cell volume contribute to the spindle checkpoint strength in
336 germline precursor cells. When we knocked down both *ani-2* and *zyg-1* in *pch-2* mutant
337 embryos, we no longer observed a significant difference (p value = 0.9096) between the
338 slopes of the regression analysis of P_1 and AB cells (Figure 4B), indicating that PCH-2 is
339 responsible for the stronger checkpoint in P_1 cells.
340
341 We observed that cell cycle timing was faster in *pch-2* mutant P_1 cells than similarly
342 sized *pch-2* mutant AB cells after treatment with *ani-2* and *zyg-1* RNAi (Figure 4B). We
343 wondered if embryonic germline precursor cells might rely on spindle checkpoint
344 proteins for normal mitotic timing, analogous to mitotically dividing stem cells in the *C.*
345 *elegans* germline (Gerhold et al., 2015) and similar to mammalian cultured cells
346 (Meraldi, 2004; Rodriguez-Bravo, 2014; Ma and Poon, 2016). To address this, we
347 measured normal mitotic timing in AB and P_1 cells of both control and *pch-2* mutant
348 embryos. We found that while normal mitotic timing is unaffected by mutation of *pch-2* in
349 AB cells, *pch-2* mutant P_1 cells go through mitosis significantly faster than control P_1
350 cells (Figure 4C), thus providing an explanation for the faster cell cycle timing in *pch-*
351 *2* mutant P_1 cells with the same cell volume as *pch-2* mutant AB cells after treatment with
352 *ani-2* and *zyg-1* RNAi.
353
354 **PCH-2's enrichment in P_1 cells is dependent on PAR-1**

355 Cell fate is driven by the asymmetric distribution of various determinants between
356 somatic and germline lineages during early divisions of the *C. elegans* embryo (reviewed
357 in Rose and Gönczy, 2014). Since we found that PCH-2 promoted the spindle
358 checkpoint strength in both AB and P_1 cells, but even more dramatically in P_1 cells, we
359 asked if PCH-2 was regulated differently between these cells. We previously generated
360 a tagged version of PCH-2 at the endogenous locus, PCH-2::GFP, that could be
361 visualized at unattached kinetochores at the pseudo-metaphase plate and rescued
362 checkpoint function in AB cells (Nelson et al., 2015). We tested whether this transgene
363 could also support the stronger checkpoint in P_1 cells. We treated embryos expressing
364 PCH-2::GFP with *zyg-1* RNAi and evaluated mitotic timing in both AB and P_1 cells, in the
365 presence or absence of monopolar spindles, using chromosome decondensation as a
366 marker for mitotic exit. P_1 cells expressing PCH-2::GFP had full checkpoint function,
367 exhibiting a mitotic delay longer than AB cells also expressing PCH-2::GFP (Figure 5A).
368
369 Previous transcriptome analysis of PCH-2 did not reveal asymmetric enrichment of PCH-
370 2 mRNA between AB and P_1 cells (Tintori et al., 2016). We tested whether PCH-2::GFP
371 exhibited differences in protein levels between AB and P_1 cells. First, we assessed
372 whether PCH-2::GFP was more enriched in pseudo-metaphase at unattached
373 kinetochores in P_1 than AB cells. We quantified PCH-2::GFP fluorescence at unattached
374 kinetochores in both AB and P_1 cells of embryos treated with *zyg-1* RNAi but did not
375 detect any difference between the two cell types (Figures S3A and B). Similarly, we did
376 not detect any difference in GFP::MAD-2 recruitment at unattached kinetochores
377 between AB and P_1 cells in *zyg-1*^{RNAi} embryos (Figures S3C and D).
378
379 Next, we quantified PCH-2::GFP fluorescence in AB and P_1 cells during unperturbed cell
380 cycles. In the AB cell, PCH-2 protein becomes enriched in the area around the

381 chromosomes in prometaphase (Nelson et al., 2015). We observed similar localization of
382 PCH-2::GFP in P_1 cells (Figure 5B). When we quantified the fluorescence of PCH-
383 2::GFP in this area surrounding chromosomes after NEBD in both AB and P_1 cells, we
384 detected a statistically significant enrichment of PCH-2::GFP in P_1 cells (Figure 5C). This
385 enrichment is not the indirect consequence of the smaller volume of P_1 cells since we did
386 not observe a difference in the fluorescence of PCH-2::GFP in the cytoplasm between
387 AB and P_1 cells (Figure S4), demonstrating that PCH-2::GFP is more highly enriched in
388 P_1 cells than AB cells.
389
390 To better understand the relationship between PCH-2 enrichment in P_1 cells and cell
391 fate, we abrogated the asymmetry of the two-cell embryo by performing RNAi against
392 the essential polarity factor, PAR-1 (Guo and Kemphues, 1995). In *par-1*^{RNAi} mutant
393 embryos, AB and P_1 cells exhibit the same checkpoint strength (Gerhold et al., 2018),
394 indicating that the stronger spindle checkpoint response in the P_1 cells depends on this
395 asymmetric division. We quantified PCH-2::GFP fluorescence in the area around
396 chromosomes in AB and P_1 cells after *par-1* RNAi and observed that the fluorescence of
397 PCH-2::GFP was not significantly different between AB and P_1 cells, unlike what we
398 observed in embryos exposed to control RNAi (Figure 5D). Therefore, PCH-2::GFP's
399 enrichment in P_1 cells depends on a conserved factor that induces embryonic
400 asymmetry and germline cell fate.
401
402 **The stronger checkpoint in P_1 cells depends on CMT-1**
403 In vitro, the *C. elegans* ortholog of p31^{comet}, CMT-1, is required for PCH-2 to bind and
404 remodel Mad2 from the closed conformation to the open one (Ye et al., 2015). In
405 addition to this role, CMT-1 is also required to localize PCH-2 to unattached
406 kinetochores during the spindle checkpoint response, stabilize Mad2 protein levels and

407 generate a robust spindle checkpoint response in AB cells (Nelson et al., 2015).
408 Overexpressing Mad2 does not suppress the partial defect in spindle checkpoint
409 activation in *cmt-1* mutants (Nelson et al., 2015), suggesting that PCH-2's localization to
410 unattached kinetochores promotes a strong spindle checkpoint response in large AB
411 cells. Therefore, we reasoned that CMT-1 might also be required for the stronger
412 checkpoint in P_1 cells.
413
414 To test this possibility, we performed *zyg-1* RNAi on control and *cmt-1* mutant embryos
415 and monitored mitotic timing in both AB and P_1 cells. AB and P_1 cells of control and *cmt-*
416 *1* mutant embryos treated with control RNAi had similar mitotic timing. In *zyg-1*^{RNAi}
417 embryos, P_1 cells exhibited a stronger checkpoint response than AB cells. By contrast,
418 both AB and P_1 cells in *cmt-1*;*zyg-1*^{RNAi} mutant embryos exhibited similar spindle
419 checkpoint delays (Figure 6A). Despite having spindle checkpoint responses that were
420 less robust than that of control *zyg-1*^{RNAi} embryos, AB and P_1 cells in *cmt-1* mutant
421 embryos treated with *zyg-1* RNAi spent significantly longer in mitosis than *cmt-1* mutant
422 embryos treated with control RNAi, indicating that they activated a weaker spindle
423 checkpoint response, similar to our published results (Nelson et al., 2015). More
424 importantly, *cmt-1*; *zyg-1*^{RNAi} mutant embryos failed to generate a stronger checkpoint in
425 P_1 cells, indicating that CMT-1 is also essential to promote checkpoint strength in
426 germline precursor cells.
427
428 Aside from localizing PCH-2 to unattached kinetochores, we wondered if CMT-1 was
429 required for any other aspects of PCH-2 regulation. Therefore, we tested whether CMT-1
430 was necessary for PCH-2's asymmetric enrichment in P_1 cells. We quantified PCH-
431 2::GFP fluorescence in prometaphase in the area around chromosomes in both *cmt-1*
432 mutant AB and P_1 cells (Figure 6B). First, we found that PCH-2::GFP fluorescence was

433 similar between AB cells in both control and *cmt-1* mutant embryos (Figure 6C),
434 consistent with our hypothesis that the weaker checkpoint in *cmt-1* AB cells is a
435 consequence of the absence of PCH-2 recruitment at unattached kinetochore (Nelson et
436 al., 2015). Further, when we compared the quantification of PCH-2::GFP fluorescence in
437 *cmt-1* mutant AB and P_1 cells, we did not detect a significant difference between the two
438 cells (Figure 6D), unlike our experiment in control embryos (Figure 5C). Thus, while we
439 favor the hypothesis that CMT-1's role in promoting spindle checkpoint strength in both
440 AB and P_1 cells is the product of localizing PCH-2 to unattached kinetochores, based on
441 the reduced robustness of the spindle checkpoint in *cmt-1* mutants (Figure 6) and our
442 *ani-2*^{RNAi}*;zyg-1*^{RNAi} experiments (Figures 1 and 2), it's likely that CMT-1's contribution to
443 the asymmetric enrichment of PCH-2 in P_1 cells also contributes to the stronger spindle
444 checkpoint in these cells.
445
446 **DISCUSSION**
447
448 The role of PCH-2, and its mammalian ortholog TRIP13, in the spindle checkpoint has
449 been enigmatic. Originally identified as a checkpoint silencing factor (Wang et al., 2014;
450 Eytan et al., 2014; Ye et al., 2015; Miniowitz-Shemtov et al., 2015; Brulotte et al., 2017;
451 Alfieri et al., 2018), more recent evidence also indicates a role in promoting the
452 checkpoint response (Nelson et al., 2015; Ma and Poon, 2016; Yost et al., 2017). It's
453 clear that the reliance on PCH-2/TRIP13 in checkpoint activation likely reflects the
454 relative levels and availability of O-Mad2 (Ma and Poon, 2018). We show here that PCH-
455 2's role in regulating O-Mad2 availability, specifically at or near unattached kinetochores,
456 also controls checkpoint strength, providing an unanticipated mechanism to explain its
457 regulation (Figure 7). We propose that this role in checkpoint strength is particularly

important in large cells, such as oocytes and cells in early embryos, as well as cells that give rise to immortal germ cells.

A prediction of our model is that overexpression of Mad2 should also make PCH-2 dispensable for the spindle checkpoint activation. We've shown that subtle elevations of Mad2 protein levels cannot suppress the requirement for PCH-2 in two-cell embryos (Nelson et al., 2015). Unfortunately, more dramatic overexpression experiments are technically difficult in *C. elegans*. Further, it's likely that strong overexpression of Mad2 in *C. elegans* embryos will delay normal mitosis, consistent with similar findings in mammalian cells (Marks et al., 2017) and budding yeast (Mariani et al., 2012). In this way, PCH-2's function may provide a useful buffer: Since Mad2 protein levels may need to stay within a narrow range to allow normal mitotic timing, PCH-2's localization at or near unattached kinetochores provide a mechanism to increase O-Mad2's local concentration to promote effective and efficient signaling during checkpoint activation.

Despite our findings that PCH-2 becomes dispensable for spindle checkpoint activation as two-cell embryos decrease in volume, PCH-2 remains essential for the spindle checkpoint as cells normally decrease in volume during embryogenesis (Figure 3), indicating that relative levels of O-Mad2 and C-Mad2 may be further regulated during embryonic development. This possibility is supported by our finding that PCH-2 regulates normal cell cycle timing in P_1 cells, but not AB cells (Figure 4C), which suggests that variations in O-Mad2/C-Mad2 ratios influence normal mitotic timing in cells with specific developmental fates. In addition, unlike the nuclei of two-cell embryos treated with *ani-2*^{RNAi} (Figure S2), nuclear volume scales with cell volume during embryogenesis (Gerhold et al., 2018). Therefore, the concentration of Mad2 may not necessarily increase as cell size decreases in cells of the developing embryo, making

484 direct comparisons between small cells obtained by *ani-2*^{RNAi} treatment and small cells
485 resulting from normal embryogenesis challenging.
486
487 Our experiments identify CMT-1, the *C. elegans* ortholog of mammalian p31^{comet}, as an
488 important regulator of PCH-2 function and, as a result, checkpoint strength. In addition to
489 its requirement in facilitating PCH-2's ability to interact with its substrate, Mad2 (Ye et al.,
490 2015; Miniowitz-Shemtov et al., 2015; Brulotte et al., 2017; Alfieri et al., 2018), CMT-1
491 localizes PCH-2 to unattached kinetochores (Nelson et al., 2015) and promotes PCH-2's
492 enrichment in P_1 cells (Figure 6). We propose that both of these roles contribute to
493 checkpoint strength. In large AB cells, CMT-1 ensures PCH-2's presence at unattached
494 kinetochores, increasing the local concentration of O-Mad2 and driving the production of
495 soluble C-Mad2 and MCC (Figure 7A). In P_1 cells, the combination of PCH-2's
496 localization at kinetochores and its enrichment promotes a checkpoint stronger than
497 somatic cells (Figure 7C). It's striking that P_1 cells, which are slightly smaller than AB
498 cells, exhibit similar checkpoint strength to AB cells when CMT-1 is absent (Figure 6).
499 This indicates that even these cells depend on PCH-2 to be present at unattached
500 kinetochores to increase the local concentration of O-Mad2 and promote checkpoint
501 strength.
502
503 Evolutionary analysis across phyla have revealed a close co-evolutionary relationship
504 between PCH-2 and its orthologs and HORMA domain containing proteins, including
505 CMT-1 and Mad2 (Vleugel et al., 2012; van Hooff et al., 2017). However, some
506 organisms that rely on the templated conversion of O-Mad2 to C-Mad2 to assemble the
507 MCC, such as budding and fission yeasts (Nezi et al., 2006; Chao et al., 2012) either
508 don't express their PCH-2 ortholog during mitosis (budding yeast) (San-Segundo and
509 Roeder, 1999) or don't have a PCH-2 ortholog in their genome (fission yeast) (Wu and

510 Burgess, 2006). This is potentially explained by cell volume: Both budding and fission
511 yeasts are two orders of magnitude smaller than mammalian cells and *C. elegans*
512 embryos. They also undergo closed mitosis, in which the nuclear envelope does not
513 break down, providing an additional opportunity to concentrate factors required for
514 mitosis. We propose that recruiting O-Mad2 to unattached kinetochores may not present
515 as great a challenge in these significantly smaller cells, making a factor required to
516 increase the local concentration of O-Mad2 at unattached kinetochores unnecessary.
517
518 An obvious question our experiments raise is how PCH-2 is enriched in P_1 cells.
519 Germline precursor cells are transcriptionally silent until gastrulation (Seydoux et al.,
520 1996) and sequencing of mRNA in early embryos shows that both CMT-1 and PCH-2
521 mRNA are not enriched in germline precursor cells (Tintori et al., 2016), indicating that
522 enrichment of PCH-2 is likely to occur at the level of protein regulation. Understanding
523 this regulation, its control by developmental events and its effect on the relative levels of
524 O-Mad2 and C-Mad2 in different cell types promises to be an exciting area of
525 investigation.
526
527 **ACKNOWLEDGEMENTS**
528
529 We would like to thank Arshad Desai, Karen Oegema, Susan Strome and David Morgan
530 for valuable strains and reagents. This work was supported by the NIH (grant numbers
531 T32GM008646 [C.R.N. and A.R.] and R01GM097144 [N.B.]). Some strains were
532 provided by the CGC, which is funded by NIH Office of Research Infrastructure
533 Programs (P40 OD010440).

534 **REFERENCES**

535 Alfieri, C., Chang, L., and Barford, D. (2018). Mechanism for remodelling of the cell cycle
536 checkpoint protein MAD2 by the ATPase TRIP13. Nature.

537 Aravind, L., and Koonin, E.V. (1998). The HORMA domain: a common structural
538 denominator in mitotic checkpoints, chromosome synapsis and DNA repair. Trends
539 Biochem. Sci. *23*, 284–286.

540 Bhalla, N., and Dernburg, A.F. (2005). A Conserved Checkpoint Monitors Meiotic
541 Chromosome Synapsis in Caenorhabditis elegans. Science *310*, 1683–1686.

542 Bohr, T., Nelson, C.R., Klee, E., and Bhalla, N. (2015). Spindle assembly checkpoint
543 proteins regulate and monitor meiotic synapsis in C. elegans. J. Cell Biol. *211*, 233–242.

544 Brenner, S. (1974). The genetics of Caenorhabditis elegans. Genetics *77*, 71–94.

545 Brulotte, M.L., Jeong, B.-C., Li, F., Li, B., Yu, E.B., Wu, Q., Brautigam, C.A., Yu, H., and
546 Luo, X. (2017). Mechanistic insight into TRIP13-catalyzed Mad2 structural transition and
547 spindle checkpoint silencing. Nat. Commun. *8*, 1956.

548 Carvalho, A., Olson, S.K., Gutierrez, E., Zhang, K., Noble, L.B., Zanin, E., Desai, A.,
549 Groisman, A., and Oegema, K. (2011). Acute drug treatment in the early C. elegans
550 embryo. PloS One *6*, e24656.

551 Chao, W.C.H., Kulkarni, K., Zhang, Z., Kong, E.H., and Barford, D. (2012). Structure of
552 the mitotic checkpoint complex. Nature *484*, 208–213.

553 Chen, C., Jomaa, A., Ortega, J., and Alani, E.E. (2014). Pch2 is a hexameric ring
554 ATPase that remodels the chromosome axis protein Hop1. Proc. Natl. Acad. Sci. U. S.
555 A. *111*, E44–E53.

556 Chen, R.H., Waters, J.C., Salmon, E.D., and Murray, A.W. (1996). Association of spindle
557 assembly checkpoint component XMAD2 with unattached kinetochores. Science *274*,
558 242–246.

559 Chen, R.H., Shevchenko, A., Mann, M., and Murray, A.W. (1998). Spindle checkpoint
560 protein Xmad1 recruits Xmad2 to unattached kinetochores. J. Cell Biol. *143*, 283–295.

561 Collin, P., Nashchekina, O., Walker, R., and Pines, J. (2013). The spindle assembly
562 checkpoint works like a rheostat rather than a toggle switch. Nat. Cell Biol. *15*, 1378–
563 1385.

564 Davis, L.I., and Blobel, G. (1986). Identification and characterization of a nuclear pore
565 complex protein. Cell *45*, 699–709.

566 De Antoni, A., Pearson, C.G., Cimini, D., Canman, J.C., Sala, V., Nezi, L., Mapelli, M.,
567 Sironi, L., Faretta, M., Salmon, E.D., et al. (2005). The Mad1/Mad2 complex as a
568 template for Mad2 activation in the spindle assembly checkpoint. Curr. Biol. CB *15*, 214–
569 225.

570 Défachelles, L., Hainline, S.G., Menant, A., Lee, L.A., and Karess, R.E. (2015). A
571 maternal effect rough deal mutation suggests that multiple pathways regulate Drosophila
572 RZZ kinetochore recruitment. J Cell Sci *128*, 1204–1216.

573 Dick, A.E., and Gerlich, D.W. (2013). Kinetic framework of spindle assembly checkpoint
574 signalling. Nat. Cell Biol. *15*, 1370–1377.

575 Edelstein, A.D., Tsuchida, M.A., Amodaj, N., Pinkard, H., Vale, R.D., and Stuurman, N.
576 (2014). Advanced methods of microscope control using μManager software. J. Biol.
577 Methods *1*.

578 Essex, A., Dammermann, A., Lewellyn, L., Oegema, K., and Desai, A. (2009).
579 Systematic analysis in Caenorhabditis elegans reveals that the spindle checkpoint is
580 composed of two largely independent branches. Mol. Biol. Cell *20*, 1252–1267.

581 Eytan, E., Wang, K., Miniowitz-Shemtov, S., Sitry-Shevah, D., Kaisari, S., Yen, T.J., Liu,
582 S.-T., and Hershko, A. (2014). Disassembly of mitotic checkpoint complexes by the joint
583 action of the AAA-ATPase TRIP13 and p31comet. Proc. Natl. Acad. Sci. U. S. A. *111*,
584 12019–12024.

585 Fava, L.L., Kaulich, M., Nigg, E.A., and Santamaria, A. (2011). Probing the in vivo
586 function of Mad1:C-Mad2 in the spindle assembly checkpoint. EMBO J. *30*, 3322–3336.

587 Galli, M., and Morgan, D.O. (2016). Cell Size Determines the Strength of the Spindle
588 Assembly Checkpoint during Embryonic Development. Dev. Cell *36*, 344–352.

589 Gerhold, A.R., Ryan, J., Vallée-Trudeau, J.-N., Dorn, J.F., Labbé, J.-C., and Maddox,
590 P.S. (2015). Investigating the regulation of stem and progenitor cell mitotic progression
591 by in situ imaging. Curr. Biol. CB *25*, 1123–1134.

592 Gerhold, A.R., Poupart, V., Labbé, J.-C., and Maddox, P.S. (2018). Spindle assembly
593 checkpoint strength is linked to cell fate in the C. elegans embryo. Mol. Biol. Cell
594 mbcE18040215.

595 Guo, S., and Kemphues, K.J. (1995). par-1, a gene required for establishing polarity in
596 C. elegans embryos, encodes a putative Ser/Thr kinase that is asymmetrically
597 distributed. Cell *81*, 611–620.

598 van Hooff, J.J., Tromer, E., van Wijk, L.M., Snel, B., and Kops, G.J. (2017). Evolutionary
599 dynamics of the kinetochore network in eukaryotes as revealed by comparative
600 genomics. EMBO Rep. *18*, 1559–1571.

601 Kyogoku, H., and Kitajima, T.S. (2017). Large Cytoplasm Is Linked to the Error-Prone
602 Nature of Oocytes. Dev. Cell *41*, 287-298.e4.

603 Lawrence, K.S., Chau, T., and Engebrecht, J. (2015). DNA damage response and
604 spindle assembly checkpoint function throughout the cell cycle to ensure genomic
605 integrity. PLoS Genet. *11*, e1005150.

606 Li, Y., and Benezra, R. (1996). Identification of a human mitotic checkpoint gene:
607 hsMAD2. Science *274*, 246–248.

608 Luo, X., Tang, Z., Rizo, J., and Yu, H. (2002). The Mad2 spindle checkpoint protein
609 undergoes similar major conformational changes upon binding to either Mad1 or Cdc20.
610 Mol. Cell *9*, 59–71.

611 Luo, X., Tang, Z., Xia, G., Wassmann, K., Matsumoto, T., Rizo, J., and Yu, H. (2004).
612 The Mad2 spindle checkpoint protein has two distinct natively folded states. Nat. Struct.
613 Mol. Biol. *11*, 338–345.

614 Ma, H.T., and Poon, R.Y.C. (2016). TRIP13 Regulates Both the Activation and
615 Inactivation of the Spindle-Assembly Checkpoint. Cell Rep. *14*, 1086–1099.

616 Ma, H.T., and Poon, R.Y.C. (2018). TRIP13 Functions in the Establishment of the
617 Spindle Assembly Checkpoint by Replenishing O-MAD2. Cell Rep. *22*, 1439–1450.

618 Maddox, A.S., Habermann, B., Desai, A., and Oegema, K. (2005). Distinct roles for two
619 C. elegans anillins in the gonad and early embryo. Dev. Camb. Engl. *132*, 2837–2848.

620 Mariani, L., Chiroli, E., Nezi, L., Muller, H., Piatti, S., Musacchio, A., and Ciliberto, A.
621 (2012). Role of the Mad2 dimerization interface in the spindle assembly checkpoint
622 independent of kinetochores. Curr. Biol. CB *22*, 1900–1908.

623 Marks, D.H., Thomas, R., Chin, Y., Shah, R., Khoo, C., and Benezra, R. (2017). Mad2
624 Overexpression Uncovers a Critical Role for TRIP13 in Mitotic Exit. Cell Rep. *19*, 1832–
625 1845.

626 Miniowitz-Shemtov, S., Eytan, E., Kaisari, S., Sitry-Shevah, D., and Hershko, A. (2015).
627 Mode of interaction of TRIP13 AAA-ATPase with the Mad2-binding protein p31comet
628 and with mitotic checkpoint complexes. Proc. Natl. Acad. Sci. U. S. A. *112*, 11536–
629 11540.

630 Moyle, M.W., Kim, T., Hattersley, N., Espeut, J., Cheerambathur, D.K., Oegema, K., and
631 Desai, A. (2014). A Bub1–Mad1 interaction targets the Mad1–Mad2 complex to
632 unattached kinetochores to initiate the spindle checkpoint. J. Cell Biol. *204*, 647–657.

633 Nelson, C.R., Hwang, T., Chen, P.-H., and Bhalla, N. (2015). TRIP13PCH-2 promotes
634 Mad2 localization to unattached kinetochores in the spindle checkpoint response. J. Cell
635 Biol. *211*, 503–516.

636 Nezi, L., Rancati, G., De Antoni, A., Pasqualato, S., Piatti, S., and Musacchio, A. (2006).
637 Accumulation of Mad2-Cdc20 complex during spindle checkpoint activation requires
638 binding of open and closed conformers of Mad2 in Saccharomyces cerevisiae. J. Cell
639 Biol. *174*, 39–51.

640 Nystul, T.G., Goldmark, J.P., Padilla, P.A., and Roth, M.B. (2003). Suspended animation
641 in C. elegans requires the spindle checkpoint. Science *302*, 1038–1041.

642 O'Connell, K.F., Caron, C., Kopish, K.R., Hurd, D.D., Kemphues, K.J., Li, Y., and White,
643 J.G. (2001). The C. elegans zyg-1 gene encodes a regulator of centrosome duplication
644 with distinct maternal and paternal roles in the embryo. Cell *105*, 547–558.

645 Rose, L., and Gönczy, P. (2014). Polarity establishment, asymmetric division and
646 segregation of fate determinants in early C. elegans embryos. WormBook Online Rev. C
647 Elegans Biol. 1–43.

648 San-Segundo, P.A., and Roeder, G.S. (1999). Pch2 links chromatin silencing to meiotic
649 checkpoint control. Cell *97*, 313–324.

650 Seydoux, G., Mello, C.C., Pettitt, J., Wood, W.B., Priess, J.R., and Fire, A. (1996).
651 Repression of gene expression in the embryonic germ lineage of C. elegans. Nature
652 *382*, 713–716.

653 Sironi, L., Melixetian, M., Faretta, M., Prosperini, E., Helin, K., and Musacchio, A. (2001).
654 Mad2 binding to Mad1 and Cdc20, rather than oligomerization, is required for the spindle
655 checkpoint. EMBO J. *20*, 6371–6382.

656 Sironi, L., Mapelli, M., Knapp, S., De Antoni, A., Jeang, K.-T., and Musacchio, A. (2002).
657 Crystal structure of the tetrameric Mad1-Mad2 core complex: implications of a "safety
658 belt" binding mechanism for the spindle checkpoint. EMBO J. *21*, 2496–2506.

659 Sudakin, V., Chan, G.K., and Yen, T.J. (2001). Checkpoint inhibition of the APC/C in
660 HeLa cells is mediated by a complex of BUBR1, BUB3, CDC20, and MAD2. J. Cell Biol.
661 *154*, 925–936.

662 Tintori, S.C., Osborne Nishimura, E., Golden, P., Lieb, J.D., and Goldstein, B. (2016). A
663 Transcriptional Lineage of the Early C. elegans Embryo. Dev. Cell *38*, 430–444.

664 Tipton, A.R., Wang, K., Oladimeji, P., Sufi, S., Gu, Z., and Liu, S.-T. (2012). Identification
665 of novel mitosis regulators through data mining with human centromere/kinetochore
666 proteins as group queries. BMC Cell Biol. *13*, 15.

667 Vader, G. (2015). Pch2(TRIP13): controlling cell division through regulation of HORMA
668 domains. Chromosoma *124*, 333–339.

669 Vleugel, M., Hoogendoorn, E., Snel, B., and Kops, G.J.P.L. (2012). Evolution and
670 function of the mitotic checkpoint. Dev. Cell *23*, 239–250.

671 Wang, K., Sturt-Gillespie, B., Hittle, J.C., Macdonald, D., Chan, G.K., Yen, T.J., and Liu,
672 S.-T. (2014). Thyroid Hormone Receptor Interacting Protein 13 (TRIP13) AAA-ATPase
673 Is a Novel Mitotic Checkpoint-silencing Protein. J. Biol. Chem. *289*, 23928–23937.

674 Wu, H.-Y., and Burgess, S.M. (2006). Two distinct surveillance mechanisms monitor
675 meiotic chromosome metabolism in budding yeast. Curr. Biol. CB *16*, 2473–2479.

676 Yang, M., Li, B., Tomchick, D.R., Machius, M., Rizo, J., Yu, H., and Luo, X. (2007).
677 p31comet blocks Mad2 activation through structural mimicry. Cell *131*, 744–755.

678 Ye, Q., Rosenberg, S.C., Moeller, A., Speir, J.A., Su, T.Y., and Corbett, K.D. (2015).
679 TRIP13 is a protein-remodeling AAA+ ATPase that catalyzes MAD2 conformation
680 switching. ELife *4*.

681 Yost, S., de Wolf, B., Hanks, S., Zachariou, A., Marcozzi, C., Clarke, M., de Voer, R.,
682 Etemad, B., Uijttewaal, E., Ramsay, E., et al. (2017). Biallelic TRIP13 mutations
683 predispose to Wilms tumor and chromosome missegregation. Nat. Genet. *49*, 1148–
684 1151.

685

686 **Figure Legends**

687

688 **Figure 1: PCH-2 becomes dispensable for the spindle checkpoint response in**

689 **somatic cells as they decrease in size**

690 (A) Images of control and *ani-2*^{RNAi} two-cell embryos. Scale bar indicates 5 μm. (B)

691 Cartoon of embryos treated with *zyg-1*^{RNAi} or *ani-2*^{RNAi}*;zyg-1*^{RNAi}. (C) Mitotic timing in AB

692 cells of control, *pch-2* and *mad-1* mutant embryos plotted against cell volume. Lines

693 represent regression analysis for each set of data. (D) Data from (C) sorted into three

694 categories: wild-type sized embryos (more than 5 x 10^3 μm^3), medium sized embryos

695 (between 3.5 x 10^3 μm^3 and 5 x 10^3 μm^3) and small embryos (less than 3.5 x 10^3 μm^3).

696 Error bars are S.E.M. In all graphs, a * indicates a p value < 0.05, ** indicates a p value

697 < 0.01 and *** a p value < 0.0001.

698

699 **Figure 2: PCH-2 becomes dispensable for MAD-2 recruitment at unattached**

700 **kinetochores in somatic cells as they decrease in size**

701 (A) Immunostaining of MAD-2 and nuclear pore complex components (NPCs) shows

702 MAD-2 localized in the nucleus and at the nuclear envelope during interphase. Scale bar

703 indicates 5 μm. (B) Cartoon and images of GFP::MAD-2 recruitment to unattached

704 kinetochores in AB cells of small embryos. Scale bar 1 μm. (C) Quantification of

705 kinetochore bound GFP::MAD-2. Error bars are S.E.M.

706

707 **Figure 3: PCH-2 is required for the spindle checkpoint response during**

708 **embryogenesis**

709 (A) Mitotic timing in control, *pch-2* and *san-1* mutant embryos treated with nocodazole at

710 different developmental stages (4- and 16-cell embryos). (B) Mitotic timing in control and

711 *pch-2* mutant embryos overexpressing GFP::MAD-2 and treated with nocodazole at
712 different developmental stages (4- and 16-cell embryos). Error bars are S.E.M.
713
714 **Figure 4: PCH-2 is responsible for the stronger spindle checkpoint in the germline**
715 **lineage**
716 Mitotic timing in AB and P_1 cells plotted against cell volume in control *ani-2*^{RNAi}*;zyg-1*^{RNAi}
717 embryos (A) or *pch-2;ani-2*^{RNAi}*;zyg-1*^{RNAi} (B) embryos. Lines represent regression
718 analysis for each set of data. (C) Unperturbed mitotic timing of AB and P_1 cells in control
719 and *pch-2* mutants. Error bars are S.E.M.
720
721 **Figure 5: PCH-2's enrichment in P_1 cells depends on PAR-1**
722 (A) Mitotic timing of control embryos and embryos expressing PCH-2::GFP during
723 unperturbed divisions or in the presence of monopolar spindles. (B) Cartoon and images
724 of PCH-2::GFP localization around mitotic chromosomes in AB and P_1 cells of two-cell
725 embryos. Scale bar indicates 5 µm. (C) Quantification of PCH-2::GFP fluorescence in
726 AB and P_1 cells. (D) Quantification of PCH-2::GFP fluorescence in AB and P_1 cells of
727 *par-1*^{RNAi} embryos. Error bars are S.E.M. NS indicates not significant.
728
729 **Figure 6: The stronger checkpoint in P_1 cells depends on CMT-1**
730 (A) Mitotic timing of control, *cmt-1* and *mad-1* mutant embryos during unperturbed
731 divisions or in the presence of monopolar spindles. (B) Cartoon and images of PCH-
732 2::GFP localization around mitotic chromosomes in AB and P_1 cells of *cmt-1* mutant
733 embryos. Scale bar indicates 5 µm. (C) Quantification of PCH-2::GFP fluorescence in
734 AB cells of control and *cmt-1* mutant embryos. (D) Quantification of PCH-2::GFP
735 fluorescence in AB and P_1 cells of *cmt-1* mutant embryos.
736

737 **Figure 7: Model**

738 (A) A robust spindle checkpoint response in large cells requires the presence of PCH-2
739 at unattached kinetochores to increase the local concentration O-MAD-2 at or near
740 unattached kinetochores. (B) Reducing cell volume of two-cell embryos increases the
741 concentration of O-Mad-2 near or at unattached kinetochores, allowing a checkpoint
742 response in the absence of PCH-2. (C) The enrichment of PCH-2 in P_1 cells results in a
743 higher production of O-MAD-2, generating a stronger spindle checkpoint response in P_1
744 cells.

745

746 **Figure S1: Related to Figure 1. The mitotic delay observed in *pch-2;ani-2^{RNAi};zyg-*
747 ***1^{RNAi}* small cells is a spindle checkpoint response.**

748 Cartoon of control and *ani-2^{RNAi}* two-cell embryos (A) and an *ani-2^{RNAi};zyg-1^{RNAi}* two-cell
749 embryo (B). Mitotic timing in AB cells plotted against cell volume, during unperturbed
750 mitosis (C) and in the presence of monopolar spindles (D). Lines represent regression
751 analysis for each set of data.

752

753 **Figure S2: Related to Figure 2. Nuclear volume does not scale with cell volume in**
754 ***ani-2^{RNAi}* two-cell embryos.**

755 (A) Images of a large (top) and small (bottom) AB cell of *ani-2^{RNAi}* embryos. The nuclear
756 area is indicated with a dashed yellow line. Scale bar indicates 5 μm (B) Nuclear area
757 plotted against cell volume.

758

759 **Figure S3: Related to Figure 5. There is no difference in the amount of PCH-2::GFP**
760 **or GFP::MAD-2 recruited to unattached kinetochores in AB and P_1 cells.**

761 (A) Cartoon and images of PCH-2::GFP recruitment to unattached kinetochores in AB
762 and P_1 cells of two-cell embryos. Scale bar indicates 1 μm. (B) Quantification of PCH-

763 2::GFP recruitment at unattached kinetochores in AB and P_1 cells. (C) Cartoon and
764 images of GFP::MAD-2 recruitment to unattached kinetochores in AB and P_1 cells of
765 two-cell embryos. Scale bar indicates 1 μm. (D) Quantification of GFP::MAD-2
766 fluorescence at unattached kinetochores in AB and P_1 cells. Error bars are S.E.M. NS
767 indicates not significant.
768
769 **Figure S4: Related to Figure 5. There is no difference in the amount of PCH-2::GFP**
770 **in the cytoplasm of AB and P_1 cells.**
771 (A) Images of AB (left) and P_1 (right) cells after NEBD. Scale bar 5 μm. (B) Quantification
772 of PCH-2::GFP fluorescence in the cytoplasm of AB and P_1 cells. Error bars are S.E.M.
773
774

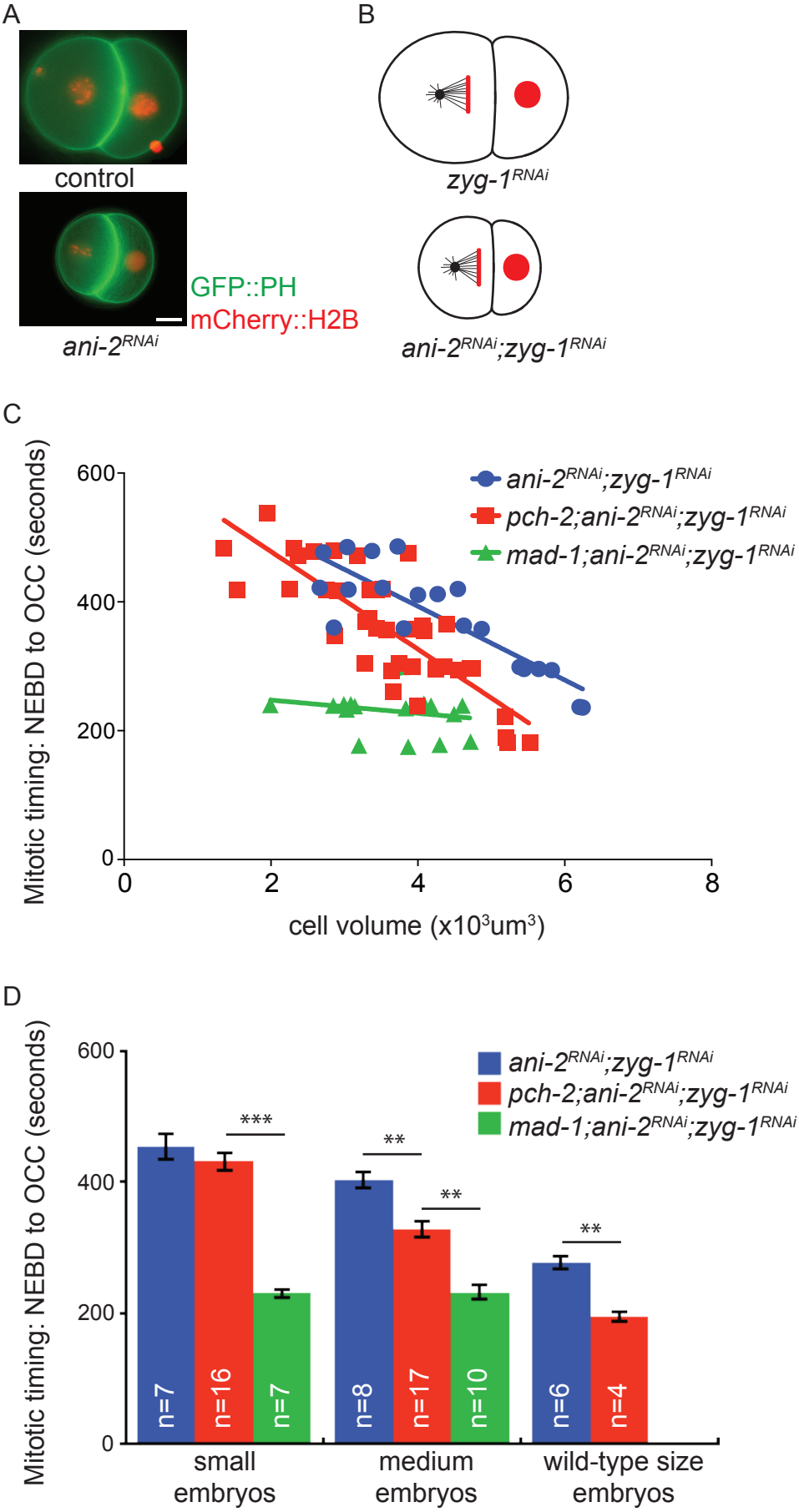
A
control
ani-2RNAi
GFP::PH
mCherry::H2B
B
zyg-1RNAi
ani-2RNAi;zyg-1RNAi
C
Mitotic timing: NEBD to OCC (seconds)
cell volume (x10³um³)
ani-2RNAi;zyg-1RNAi
pch-2;ani-2RNAi;zyg-1RNAi
mad-1;ani-2RNAi;zyg-1RNAi
D
Mitotic timing: NEBD to OCC (seconds)
***
**
**
**
n=7
n=16
n=7
n=8
n=17
n=10
n=6
n=4
small embryos
medium embryos
wild-type size embryos

A

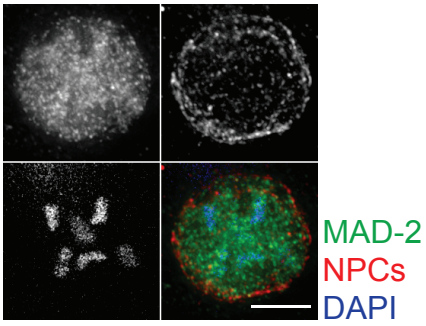
MAD-2
NPCs
DAPI

B

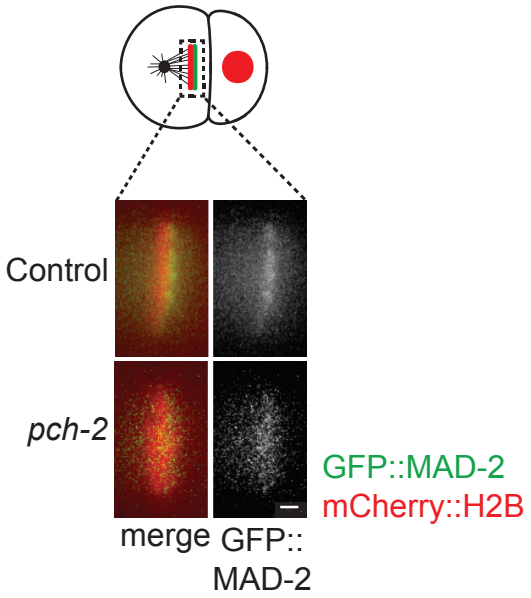
Control
pch-2
merge
GFP::
MAD-2
GFP::MAD-2
mCherry::H2B

C

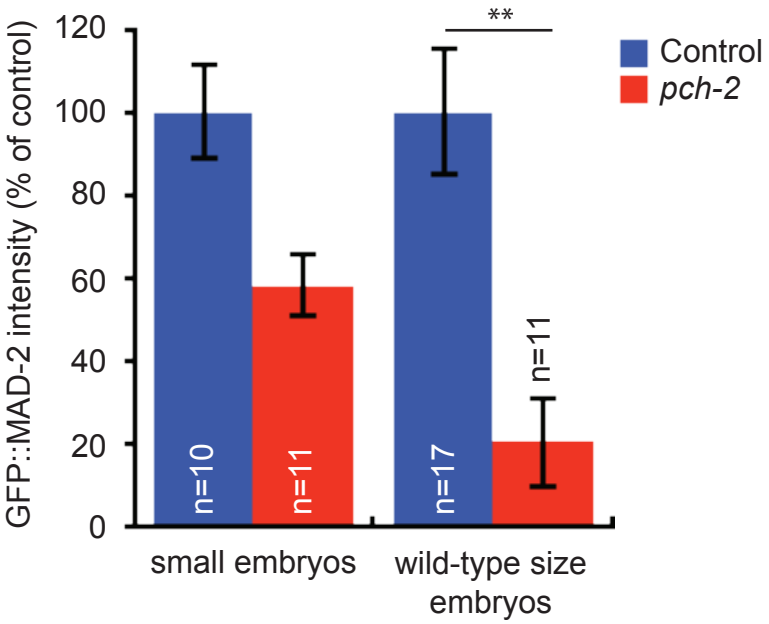
GFP::MAD-2 intensity (% of control)
120
100
80
60
40
20
0
**
Control
pch-2
n=10
n=11
n=17
n=11
small embryos
wild-type size
embryos

Défachelles et. al., Figure 3

A

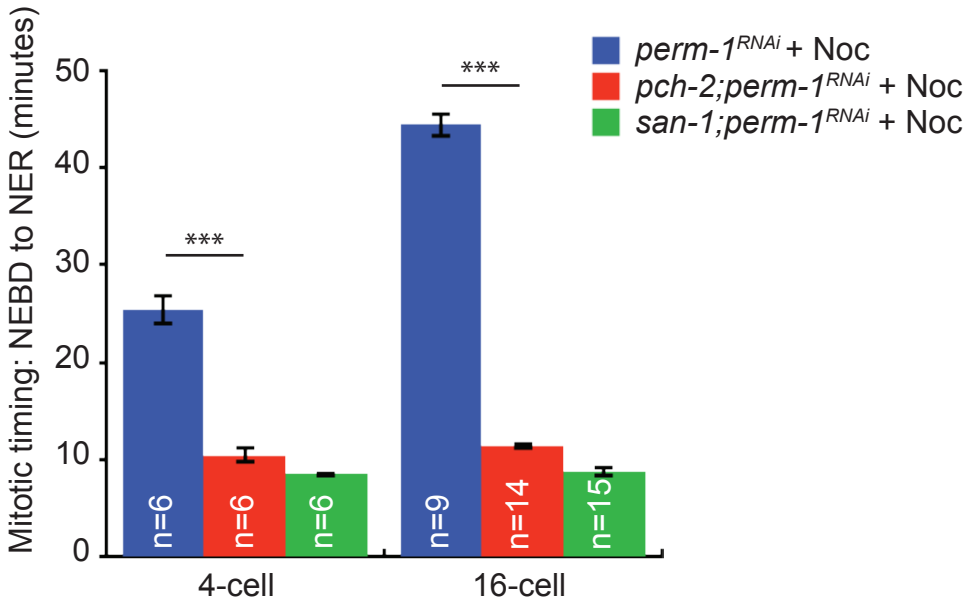

B

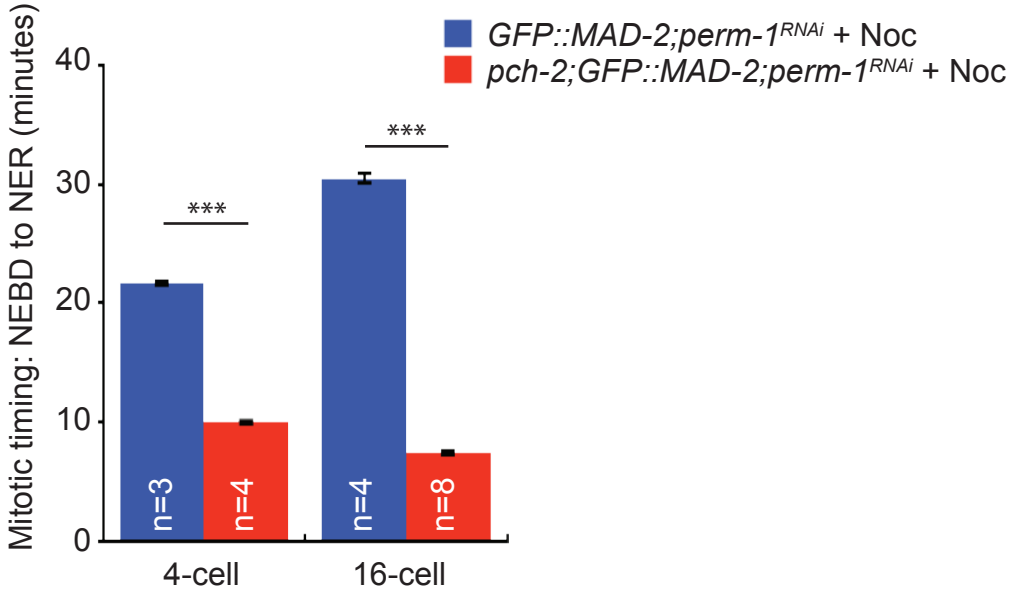

A

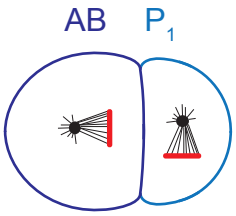
AB
P1

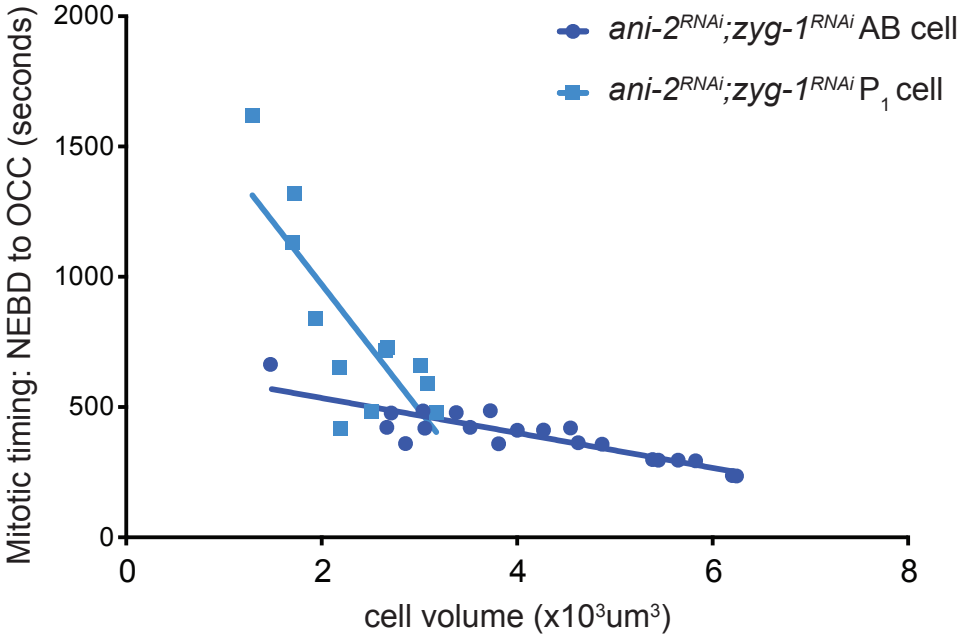
ani-2RNAi;zyg-1RNAi AB cell
ani-2RNAi;zyg-1RNAi P1 cell
Mitotic timing: NEBD to OCC (seconds)
2000
1500
1000
500
0
0
2
4
6
8
cell volume (x10³um³)

B

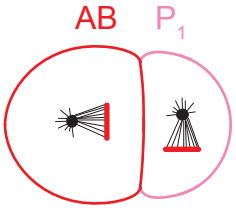
AB
P1

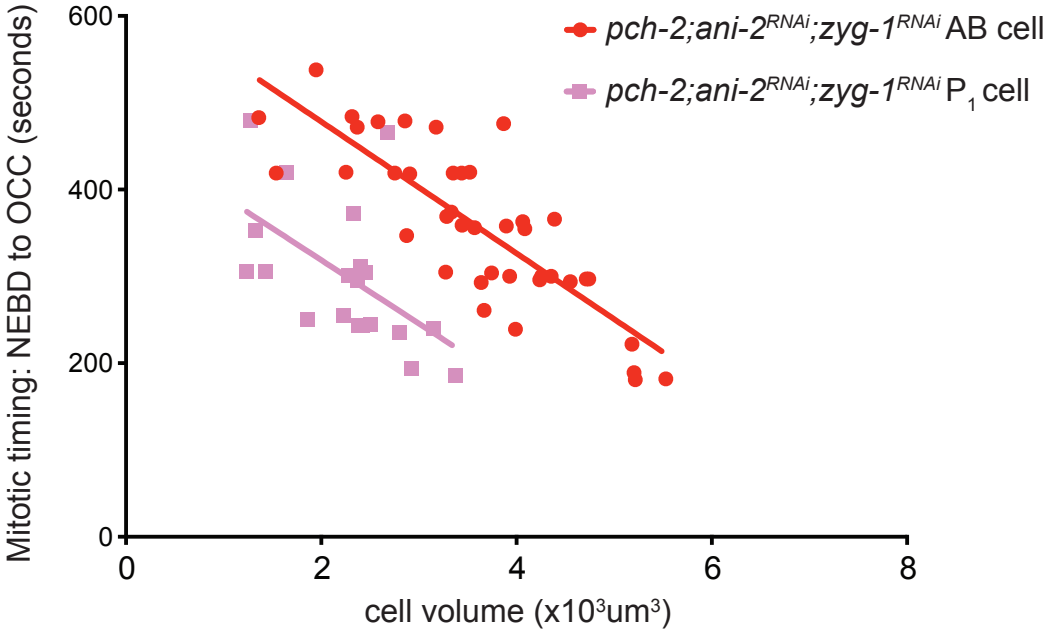
pch-2;ani-2RNAi;zyg-1RNAi AB cell
pch-2;ani-2RNAi;zyg-1RNAi P1 cell
Mitotic timing: NEBD to OCC (seconds)
600
400
200
0
0
2
4
6
8
cell volume (x10³um³)

C

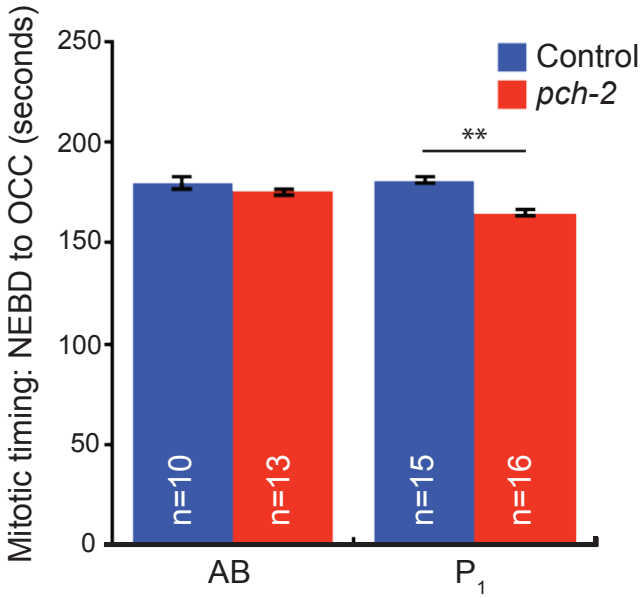
Control
pch-2
**
Mitotic timing: NEBD to OCC (seconds)
250
200
150
100
50
0
n=10
n=13
n=15
n=16
AB
P1

Défachelles et. al., Figure 5

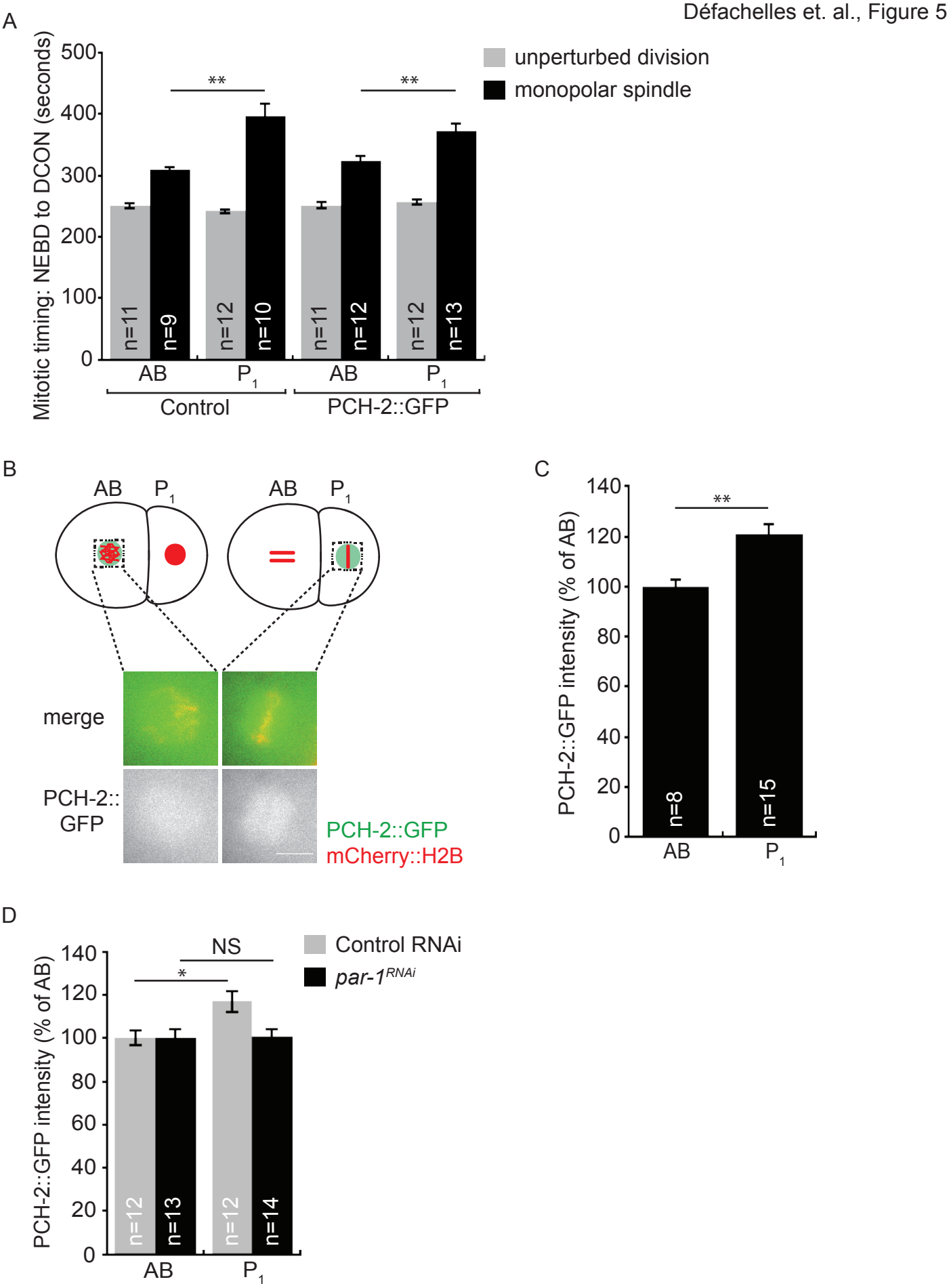

Défachelles et. al., Figure 6

A

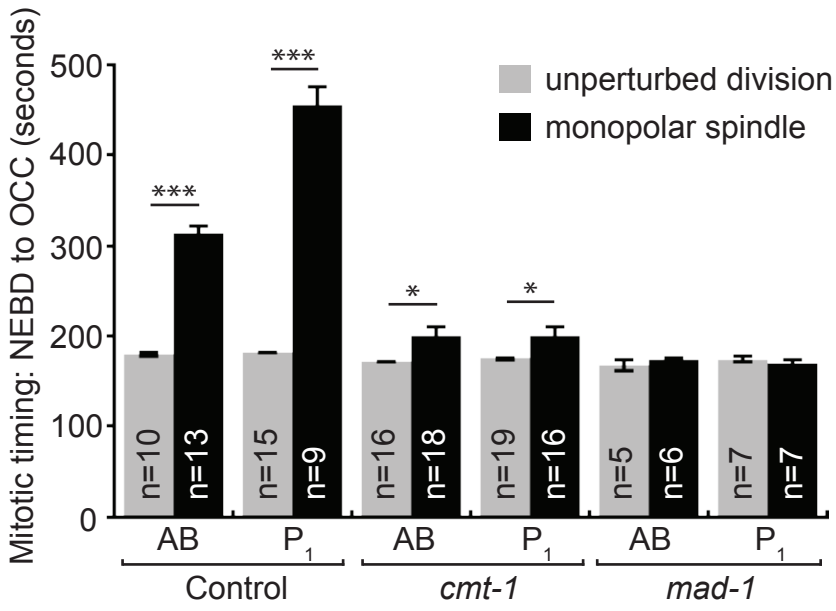

B

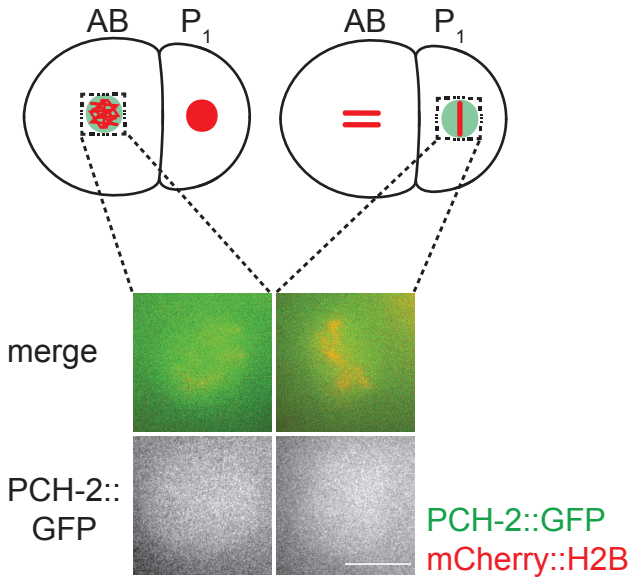

C

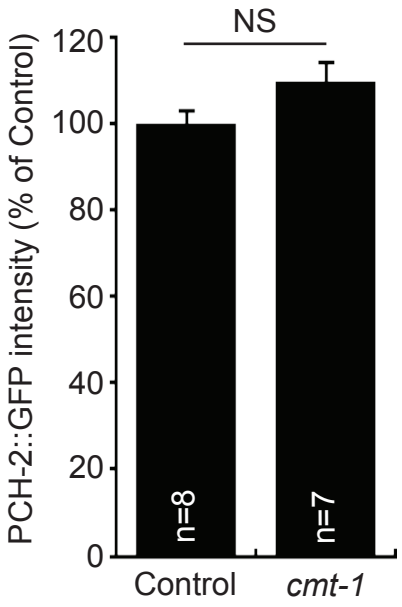

D

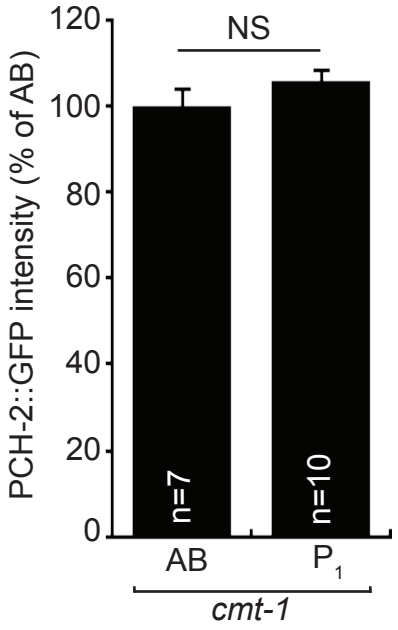

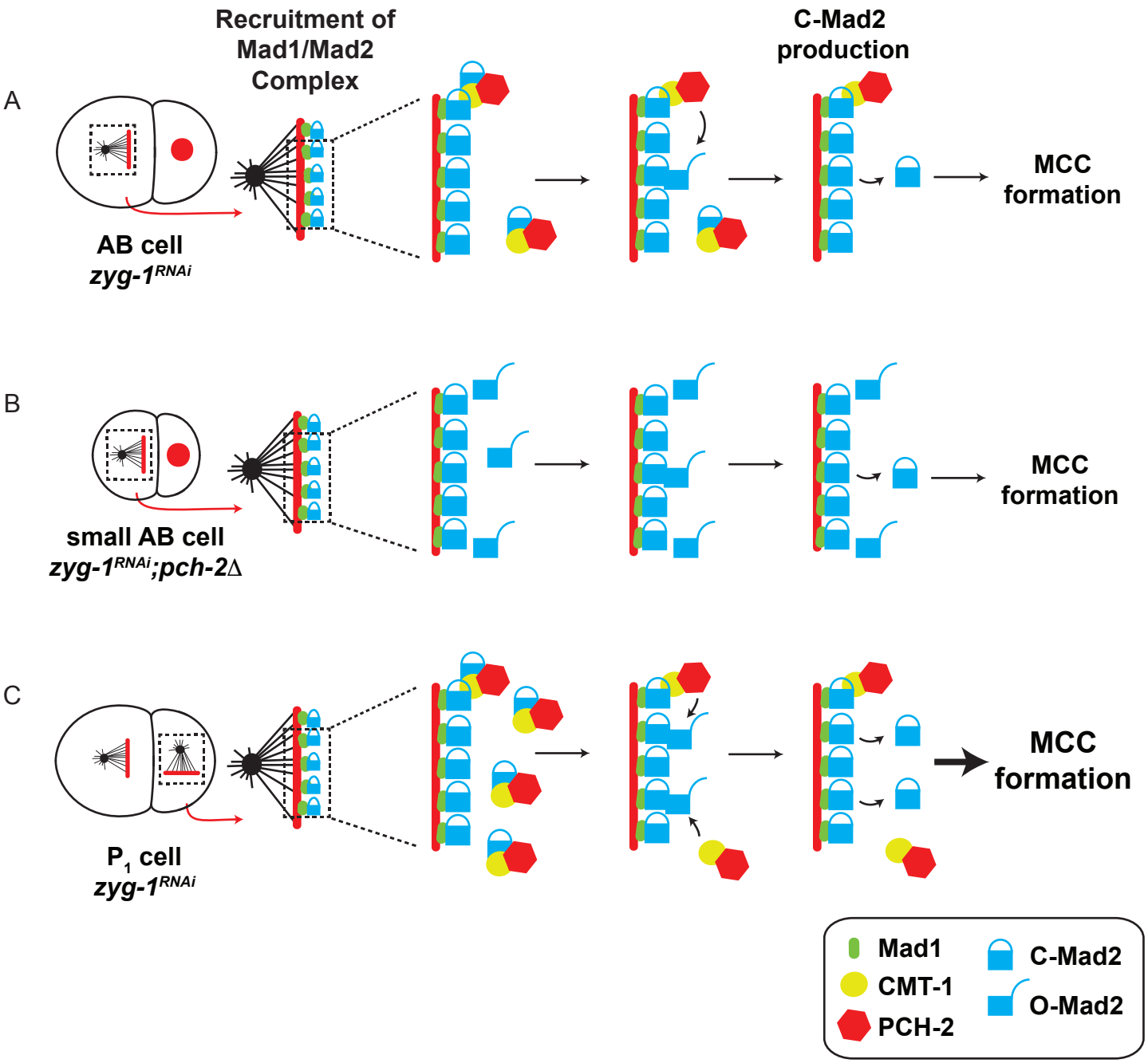
A
Recruitment of
Mad1/Mad2
Complex
C-Mad2
production
AB cell
zyg-1RNAi
MCC
formation
B
small AB cell
zyg-1RNAi;pch-2Δ
MCC
formation
C
P1 cell
zyg-1RNAi
MCC
formation
Mad1
CMT-1
PCH-2
C-Mad2
O-Mad2

Strain	Genotype
OD56	*unc-119(ed3) III; ltIs37 [pAA64; Ppie-1::mCherry::his-58; unc-119 (+)] IV*
OD95	*unc-119(ed3) III; ltIs37 [pAA64; Ppie-1::mCherry::his-58; unc-119 (+)] IV; ltIs38 [pAA1; Ppie-1::GFP::PH(PLC1delta1); unc-119(+)]*
BHL575	*pch-2(tm1458) II; unc-119(ed3) III; ltIs37 [pAA64; Ppie-1::mCherry::his-58; unc-119 (+)] IV; ltIs38 [pAA1;Ppie-1::GFP::PH(PLC1delta1); unc-119(+)]*
BHL596	*unc-119(ed3) III; ltIs37 [pAA64; Ppie-1::mCherry::his-58; unc-119 (+)] IV; ltIs38 [pAA1; Ppie-1::GFP::PH(PLC1delta1); unc-119(+)]; mdf-1(av19) V*
BHL600	*unc-119(ed3) III; ltIs37 [pAA64; Ppie-1::mCherry::his-58; unc-119 (+)] IV; ltIs52 [pOD379; Ppie-1::GFP::MDF-2; unc-119 (+)]*
BHL604	*pch-2(tm1458) II; unc-119(ed3) III; ltIs37 [pAA64; Ppie-1::mCherry::his-58; unc-119 (+)] IV; ltIs52 [pOD379; Ppie-1::GFP::MDF-2; unc-119 (+)]*
BHL608	*cmt-1(ok2879) I; unc-119(ed3) III; ltIs37 [pAA64; Ppie-1::mCherry::his-58; unc-119 (+)] IV; ltIs38 [pAA1;Ppie-1::GFP::PH(PLC1delta1); unc-119(+)]*
BHL664	*Ppch-2::pch-2::GFP-3XFLAG (blt4 [pCN94]) II; unc-119(ed3) III; ltIs37 [pAA64; Ppie-1::mCherry::his-58; unc-119 (+)] IV*
BHL883	*san-1/mdf-3 (ok1580) I; pch-2(tm1458) II; unc-119(ed3) III; ltIs37 [pAA64; Ppie-1::mCherry::his-58; unc-119 (+)] IV; ltIs38 [pAA1; Ppie-1::GFP::PH(PLC1delta1); unc-119(+)]*
BHL887	*cmt-1(ok2879) I; pch-2::GFP-3XFLAG (blt4 [pCN94]) II; unc-119(ed3) III; ltIs44[pAA173; pPie-1::mCherry::PH(PLC1delta1); unc-119(+)]; ltIs37 [pAA64; Ppie-1::mCherry::his-58; unc-119 (+)] IV*
BHL888	*unc-119(ed3) III; ltIs44 [pAA173; pPie-1::mCherry::PH(PLC1delta1); unc-119(+)]; ltIs52 [pOD379; Ppie-1::GFP::mdf-2; unc-119 (+)]; ltIs37 [pAA64; Ppie-1::mCherry::his-58; unc-119 (+)] IV*
BHL889	*pch-2(tm1458) II; unc-119(ed3) III; ltIs44 [pAA173; pPie-1::mCherry::PH(PLC1delta1); unc-119(+)]; ltIs52 [pOD379; Ppie-1::GFP::mdf-2; unc-119 (+)]; ltIs37 [pAA64; Ppie-1::mCherry::his-58; unc-119 (+)] IV*
BHL891	*unc-119(ed3) III; ltIs37 [pAA64; Ppie-1::mCherry::his-58; unc-119 (+)] IV; ltIs24[pAZ132; pPie-1::GFP::tba-2; unc-119(+)]*
BHL892	*pch-2 (tm1458) II; unc-119(ed3) III; ltIs37 [pAA64; Ppie-1::mCherry::his-58; unc-119 (+)] IV; ltIs24 [pAZ132; pPie-1::GFP::tba-2; unc-119(+)]*
BHL893	*san-1/mdf-3 (ok1580) I; unc-119(ed3) III; ltIs37 [pAA64; Ppie-1::mCherry::his-58; unc-119 (+)] IV; ltIs38 [pAA1; Ppie-1::GFP::PH(PLC1delta1); unc-119(+)]*
BHL904	*Ppch-2::pch-2::GFP-3XFLAG (blt4 [pCN94]) II; unc-119(ed3) III; ltIs44[pAA173; pPie-1::mCherry::PH(PLC1delta1); unc-119(+)]; ltIs37 [pAA64; Ppie-1::mCherry::his-58; unc-119 (+)] IV*
GAL5	*san-1/mdf-3 (mat5) I; unc-119(ed3) III; ruIs57[Ppie-1::GFP::tubulin + unc-119(+)]; ltIs37[pie-1p::mCherry::his-58 (pAA64) + unc-119(+)] IV*

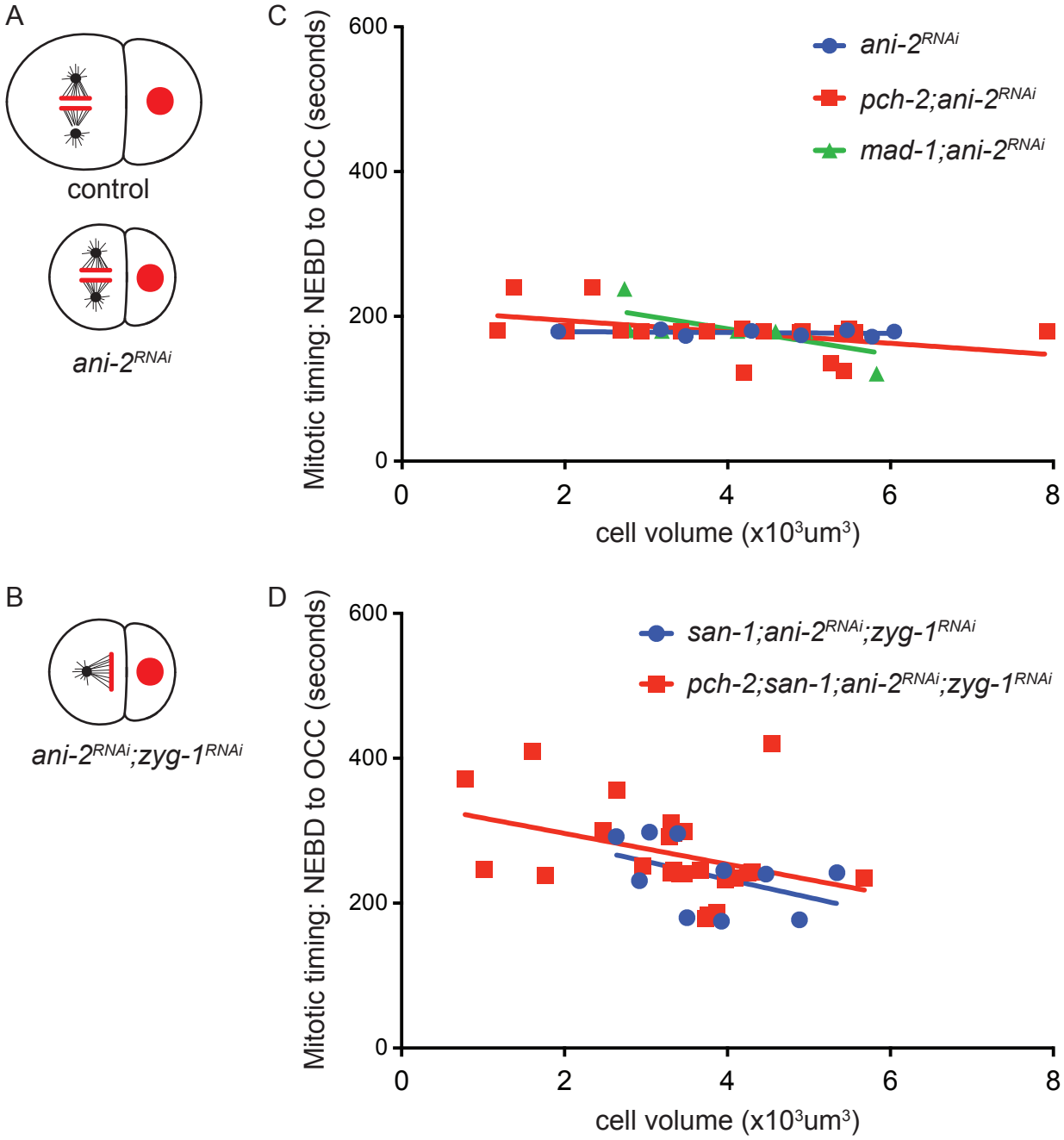
A
control
ani-2RNAi
B
ani-2RNAi;zyg-1RNAi
C
Mitotic timing: NEBD to OCC (seconds)
600
400
200
0
0
2
4
6
8
cell volume (x10³um³)
ani-2RNAi
pch-2;ani-2RNAi
mad-1;ani-2RNAi
D
Mitotic timing: NEBD to OCC (seconds)
600
400
200
0
0
2
4
6
8
cell volume (x10³um³)
san-1;ani-2RNAi;zyg-1RNAi
pch-2;san-1;ani-2RNAi;zyg-1RNAi

Défachelles et. al., Figure S2

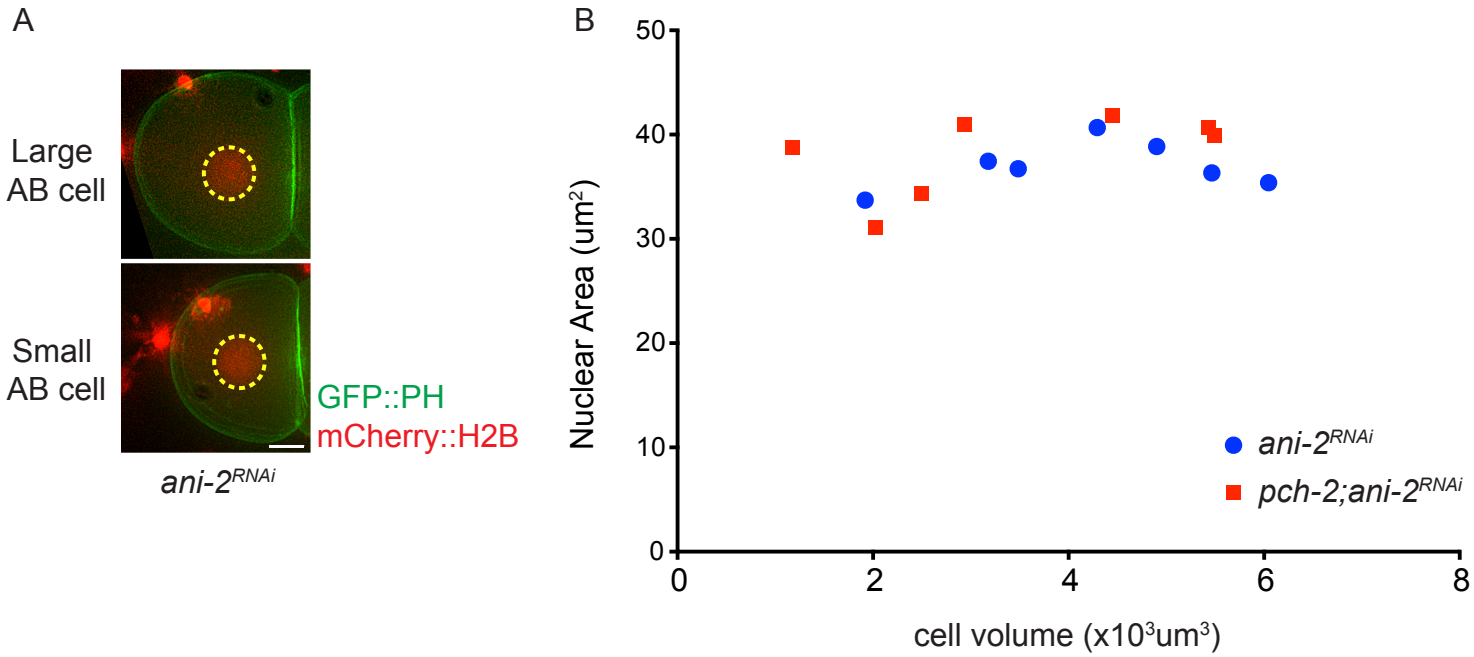

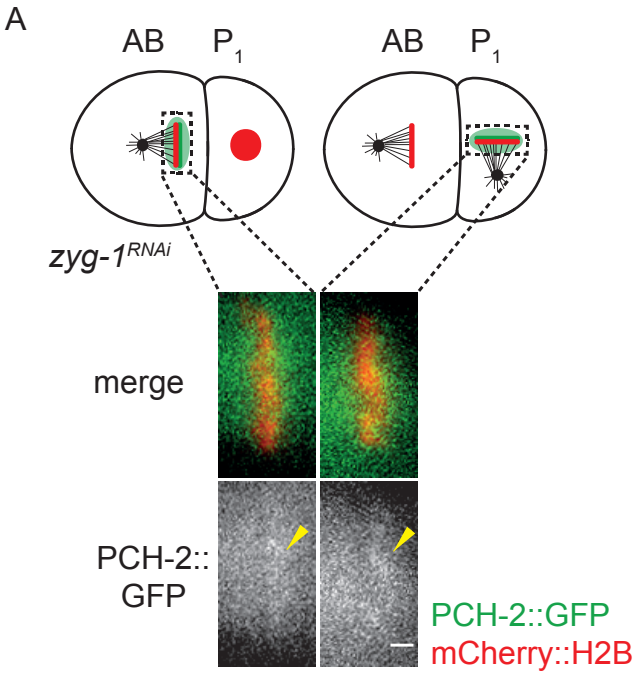
A
AB
P1
AB
P1
zyg-1RNAi
merge
PCH-2::
GFP
PCH-2::GFP
mCherry::H2B

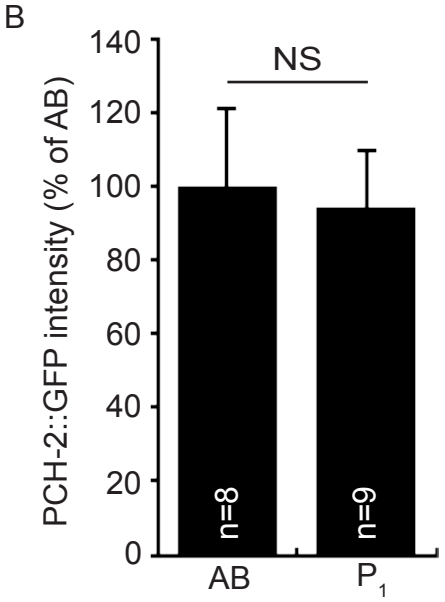
B
NS
PCH-2::GFP intensity (% of AB)
140
120
100
80
60
40
20
0
n=8
n=9
AB
P1

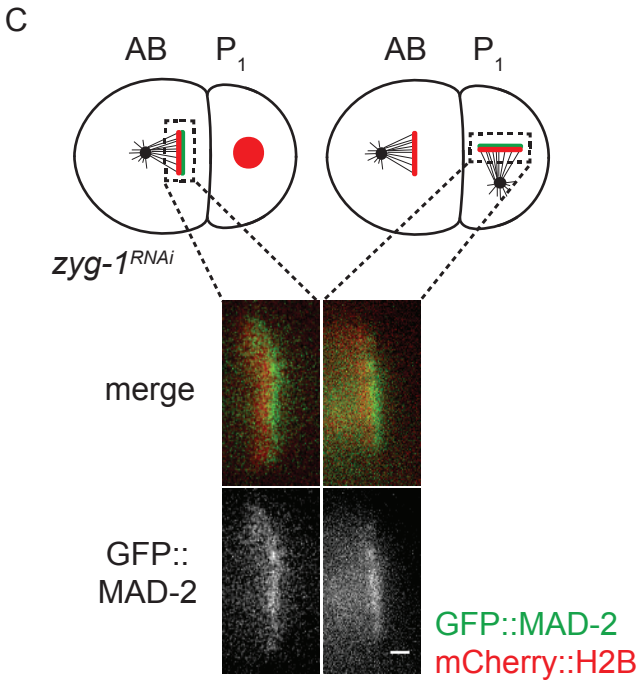
C
AB
P1
AB
P1
zyg-1RNAi
merge
GFP::
MAD-2
GFP::MAD-2
mCherry::H2B

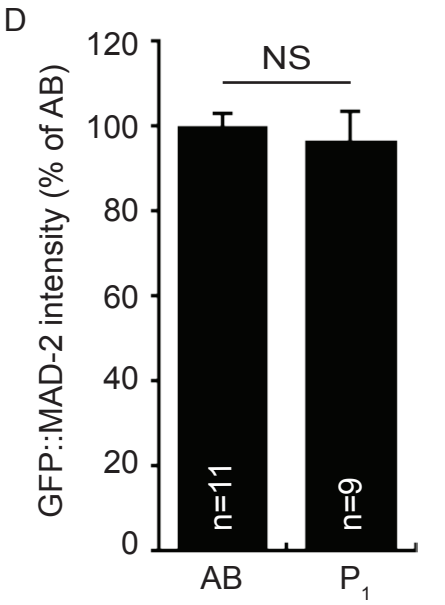
D
NS
GFP::MAD-2 intensity (% of AB)
120
100
80
60
40
20
0
n=11
n=9
AB
P1

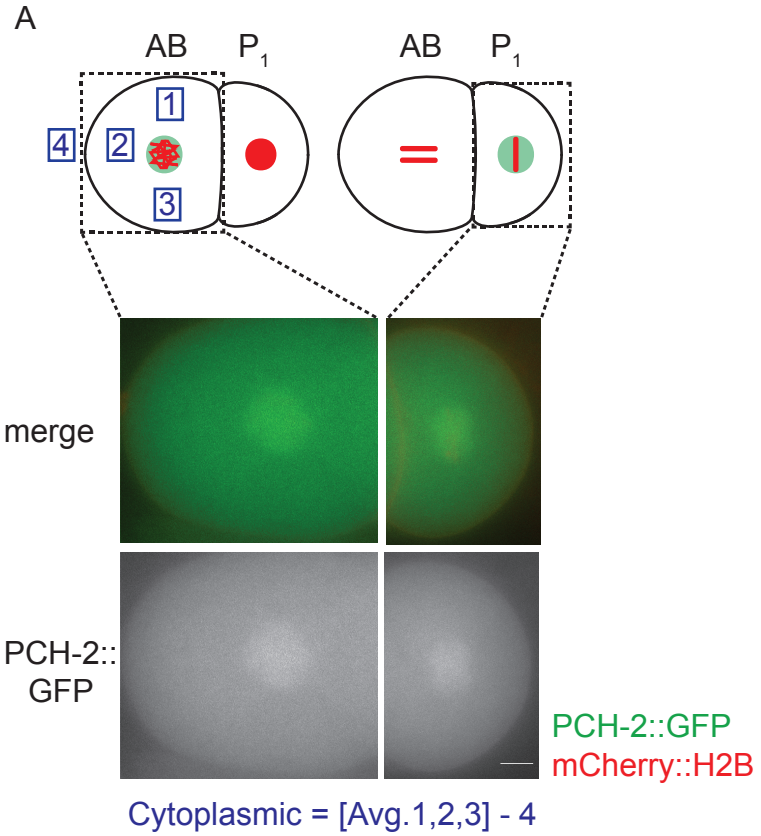
A
AB
P1
AB
P1
1
2
3
4
merge
PCH-2::
GFP
PCH-2::GFP
mCherry::H2B
Cytoplasmic = [Avg.1,2,3] - 4

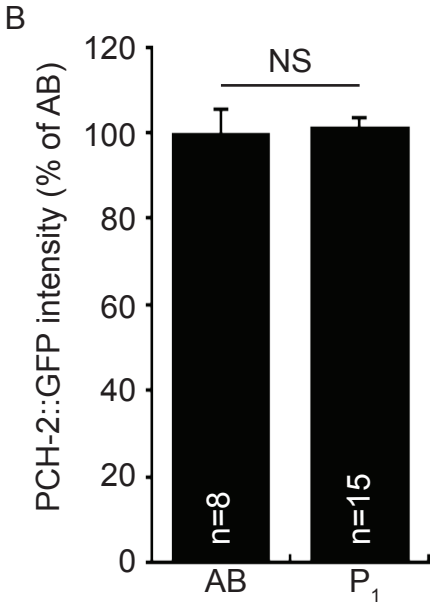
B
PCH-2::GFP intensity (% of AB)
120
100
80
60
40
20
0
NS
n=8
n=15
AB
P1